JGR Planets

RESEARCH ARTICLE
10.1029/2023JE008090

Nanoscale Spectroscopic Identification and Characterization of Minerals and Organic Matter in Ryugu Particles

Mehmet Yesiltas[1], Timothy D. Glotch[1], Yoko Kebukawa[2], Bogdan Sava[3], Yasin C. Durmaz[3,4], and Paul Northrup[1]

[1]Department of Geosciences, Stony Brook University, Stony Brook, NY, USA, [2]Department of Earth & Planetary Sciences, Tokyo Institute of Technology, Tokyo, Japan, [3]Attocube Systems, Haar, Germany, [4]Department of Physics, Ludwig Maximilians University of Munich, Munich, Germany

Key Points:

- Nanoscale mineralogy and organic matter content of Ryugu asteroid particles have been determined
- The investigated Ryugu particles have been determined to be highly rich in organic matter, and present complex organic chemistry
- Ryugu particles show incomplete and heterogeneous aqueous alteration and experience minimal and varying thermal metamorphism

Supporting Information:

Supporting Information may be found in the online version of this article.

Correspondence to:

M. Yesiltas,
mehmet.yesiltas@stonybrook.edu

Citation:

Yesiltas, M., Glotch, T. D., Kebukawa, Y., Sava, B., Durmaz, Y. C., & Northrup, P. (2024). Nanoscale spectroscopic identification and characterization of minerals and organic matter in Ryugu particles. *Journal of Geophysical Research: Planets*, *129*, e2023JE008090. https://doi.org/10.1029/2023JE008090

Received 6 SEP 2023
Accepted 15 MAR 2024

Abstract Carbonaceous asteroids are leftover materials from the early solar system. They did not undergo planetary differentiation processes and thus still retained signatures and clues of the origin and evolution of the solar system. Thus, samples of carbonaceous asteroids provide significant potential for deciphering the origin of the solar system. The Hayabusa2 spacecraft returned the first samples of a carbonaceous asteroid (162173) Ryugu. In this work, we report the nanoscale mineralogy and organic matter content of two Ryugu particles, A0030 and C0034. These were analyzed by highly novel scattering-type scanning near-field optical microscopy (s-SNOM)-based nanoscale-Fourier transform infrared (nano-FTIR) spectroscopy with ∼20 nm spatial resolution. The nano-FTIR measurements were supported by confocal micro-Raman imaging and spectroscopy (∼500 nm/pixel spatial sampling). Our investigations show that the two Ryugu particles (a) contain different silicate mineralogies, indicating heterogeneous and incomplete aqueous alteration and (b) are highly rich in organic matter, consisting a variety of molecular functional groups. The spatial distributions of chemical functional groups and their associations based on pseudo-heterodyne (PsHet) SNOM imaging show that the organic matter is distributed as either diffused or discrete grains. Micro-Raman spectra show that the Ryugu particles experienced minimal thermal metamorphism, although A0030 was slightly more heated than C0034. The identification of abundant nanoscale organic molecules within the Ryugu grains that could not be identified via micrometer-scale investigations emphasizes the importance of using nanoscale nondestructive methods for studying primitive solar system materials, such as Ryugu and OSIRIS-Rex particles and those that will be returned in the future (such as MMX samples).

Plain Language Summary Asteroids are left over materials from the early formation of our solar system ∼4.57 billion years ago. Carbonaceous asteroids contain minerals that are capable of synthesizing a variety of organic molecules. Indeed, carbonaceous asteroids contain abundant organic matter. For the first time, samples of a carbonaceous asteroid Ryugu were returned to Earth by JAXA in late 2020. The returned asteroid samples provided uncontaminated pristine organic compositions. Investigations of Ryugu samples can provide clues to understanding planet formation processes as well as the origin and evolution of the early solar system. We show the chemical composition of two Ryugu particles determined by highly novel multiscale spectroscopic and microscopic methods. Nanoscale infrared spectroscopy shows the presence of different phyllosilicate mineralogies, indicative of incomplete and heterogeneous aqueous alteration in the parent asteroid. Our results also show the presence of abundant and heterogeneous organic matter with different structural properties (diffuse vs. discrete) in the Ryugu particles, which are due to complex formation and evolution of these molecules.

1. Introduction

Carbonaceous asteroids are leftover materials from the early solar system. They can provide clues to understanding planet formation processes as well as the origin and evolution of the early solar system. Their organic compositions especially provide significant potential for deciphering the origin of our own solar system because they contain primitive materials such as minerals and organic materials that did not undergo high temperature planetary differentiation processes. The Hayabusa2 spacecraft of the Japan Aerospace Exploration Agency (JAXA) sampled two different locations from the near-Earth carbonaceous asteroid (162173) Ryugu, collecting a total of ∼5.4 g of asteroid sample, and returned the samples to Earth on 6 December 2020 for detailed laboratory analyses (Tachibana et al., 2022; Yada et al., 2022). The spacecraft collected surface regolith material (stored in

Chamber A) from the first site, referred to as touchdown location 1 (TD1), whereas it collected subsurface material (stored in Chamber C) from the second site, referred to as touchdown location 2 (TD2). Notably, some surface material could have been incorporated into Chamber C as well during the sample collection. The returned pristine asteroid samples are highly valuable because they could help us reveal and constrain the history of the parent body of Ryugu. The returned samples also provide uncontaminated pristine organic compositions that were otherwise inaccessible because meteorites always have the risk of contamination and are chemically and physically modified by interaction with the terrestrial environment. Initial characterizations showed that Ryugu samples contain abundant phyllosilicates (~64–88 vol%) (Ito et al., 2022), and are compositionally most similar to Ivuna-type carbonaceous chondrites (Greenwood et al., 2023; Nakamura, Kobayashi, et al., 2022; Pilorget et al., 2022; Yada et al., 2022; Yokoyama et al., 2022). Other components of Ryugu samples include carbonates, sulfides, and magnetite (Ito et al., 2022). Macromolecular organic matter (OM) in Ryugu samples includes aromatic carbons, aliphatic carbons, ketones, and carboxyls (Yabuta et al., 2023). Naraoka et al. (2023) reported the presence of a diverse suite of soluble organic matter in Ryugu particles resembling CI chondrites. Ryugu particles also contain presolar silicate grains, SiC, and isotopically anomalous organic matter (Barosch et al., 2022; Nguyen et al., 2023). The organic matter (submicrometer to nanometer in size) in the carbon-rich clasts (exogenous solid objects) have higher N than that of the Ryugu matrix, and these N-rich organic matter potentially formed in the outer solar system and likely in the different parts of the molecular cloud than the bulk Ryugu (Nguyen et al., 2023). Dartois et al. (2023) reported conventional hyperspectral IR maps (at a 6 μm × 6 μm sampling window with a step size of ~3 μm) to show the variations in the chemical functional groups and their spatial associations.

Extraterrestrial organic matter is typically submicron in size, and most organic compounds (e.g., carbonyls, hydrocarbons, etc.) are even smaller (De Gregorio et al., 2013; Garvie et al., 2008; Nakamura-Messenger et al., 2006; Yesiltas, Glotch, & Sava, 2021). Spatial resolution of conventional IR methods generally varies from >5 μm (Dartois et al., 2023) to 25 μm (Morlok et al., 2020), and it goes down to ~1 μm if multi-beam synchrotron radiation and array detectors are used (Nasse et al., 2011; Yesiltas et al., 2014; Yesiltas & Kebukawa, 2016). Thus, conventional IR methods cannot be used to detect and identify spectral signatures of nanoscale organic matter in situ in extraterrestrial samples because of their insufficient spatial resolution and various other technical limitations (such as optical diffraction limit, wavelength dependence). Novel analytical techniques with nanoscale spatial resolution are clearly required to detect and characterize this organic matter within extraterrestrial astromaterials, such as returned samples from asteroids and other planetary bodies. Scattering-type near-field optical microscopy (s-SNOM)-based nanoscale Fourier transform infrared (nano-FTIR) spectroscopy is a robust and useful technique providing exceptional spatial resolution down to 5 nm (Mastel et al., 2018) and detection capabilities without the optical limitations of conventional IR spectroscopy (Amarie et al., 2012; Huth et al., 2012; Yesiltas, Glotch, & Kaya, 2021; Yesiltas, Glotch, & Sava, 2021; Young et al., 2022). By utilizing an apertureless near-field optical microscope, both the essential information and the background signals arising from sources like the AFM tip shaft and far-field emissions from the sample under examination are captured. We utilized the neaSCOPE (attocube systems) that employs s-SNOM technology to effectively eliminate these undesirable background artifact signals, ensuring a precise and focused collection of the desired information. Ocelic et al. (2006) introduced pseudoheterodyne (PsHet) detection for background-free near-field spectroscopy based on the phase modulation of the reference wave, which enables unambiguous nanoscale imaging of near-field optical amplitude and phase contrasts and thus artifact- and background-free IR maps.

In this study, we investigated the mineralogy and organic matter content of two Ryugu particles, A0030 (surface sample from TD1 and Chamber A) and C0034 (subsurface sample from TD2 and Chamber C), using s-SNOM-based nano-FTIR spectroscopy, PsHet s-SNOM imaging, confocal micro-Raman spectroscopy, and conventional micro-FTIR spectroscopy. Here, we present our detailed nanoscale (~20 nm spatial resolution) detection and identification of phyllosilicates, carbonates, and organic matter. Wavelength-specific IR absorption maps collected by utilizing the highly sensitive pseudoheterodyne detection principle show the relative distribution of the different molecular groups and their spatial relationships in both Ryugu particles. Micro-Raman imaging datasets show the extent of their thermal metamorphic history.

2. Materials and Methods

2.1. Samples

Two Ryugu particles, A0030 and C0034, were loaned to us by JAXA through the first announcement of opportunity (AO1). We prepared a sulfur-embedded sample from both A0030 and C0034 particles using very small (~50 μm diameter) fragments for testing the instruments and measurement modes.

For micro-FTIR spectroscopy, small chips were carefully separated from these larger grains and transferred to chemical vapor deposition (CVD) diamond windows (3.5 mm diameter and 0.3 mm thick) using a stainless steel needle under a binocular microscope, then pressed between two diamond windows by hand to flatten the grain surface at an appropriate thickness. After separation of the two diamond windows, usually the samples are evenly distributed on both windows.

Prior to the nano-FTIR and micro-Raman measurements, an interior chip from both large Ryugu samples was broken off and pressed between clean diamond windows individually, creating a large and flat surface for spectroscopic imaging experiments for each Ryugu sample. The sample preparation processes were conducted under a clean hood, or a clean bench installed in a clean booth under clean air filtered by HEPA filters in a class 10,000 cleanroom. All results presented here are from the flat diamond-pressed surfaces, with the exception of those in Figures 7 and 11, which are from one of the sulfur-embedded fragments. The prepared Ryugu samples were studied via s-SNOM nano-FTIR spectroscopy, s-SNOM PsHet imaging, and micro-Raman spectroscopy and imaging. For comparison, micro-Raman spectra were also collected from a petrologic type-1 chondrite (Orgueil), type-2 chondrites consisting of four CM2 (Allan Hills (ALH) 85005, Yamato (Y) 980039, Asuka (A) 12236, Aguas Zarcas) and a CR2 chondrite (Graves Nunataks (GRA) 95229). In addition, Raman spectral parameters of type-3 chondrites consisting of 12 CO and 12 CV chondrites (from Yesiltas, Young, & Glotch, 2021) were used here for comparison and collected using the same Raman instrument.

2.2. Nano-FTIR Spectroscopy

Scattering-type near-field optical microscope (s-SNOM)-based nanoscale Fourier transform infrared (nano-FTIR) spectroscopic experiments were conducted using a commercial nano-FTIR imaging system (neaSCOPE, attocube.com). The system was equipped with multiple mid-infrared broadband laser sources for collecting spectra within the 1,300–750 cm^{-1} (7.7–13.3 μm) and 1,850–1,100 cm^{-1} (5.5–9.1 μm) regions. Nano-FTIR spectra were collected with ~20 nm spatial and 10 cm^{-1} spectral resolution from selected areas/points on the surface of samples. A PtIr-coated neaspec cantilever AFM tip (258 kHz tip frequency, 300 mV tip amplitude, and ~60 nm tapping amplitude) was used for recording the data. Each spectrum is the result of averaging seven individual spectra, each acquired over a 10-s interval. A silicon wafer was measured as a reference with the same experimental settings. The Michelson interferometer within the nano-FTIR system simultaneously generated amplitude and phase spectra, which represent reflection and absorption, respectively. Previous studies have shown that near-field phase spectra match well with the absorption of organic materials (Amarie et al., 2009; Huth et al., 2011, 2012). As such, phase spectra are reported in this study, as they could be interpreted as the infrared absorbance. Each nano-FTIR measurement also generated mechanical amplitude and optical amplitude images. The mechanical amplitude represents the height of the AFM tip relative to the sample surface, whereas the optical amplitude is the integrated spectral signal representing the broadband reflectivity of the sample integrated across the full wavelength range of the utilized laser. We ensured the reproducibility of the spectra by measuring the same point twice in a region of interest, one at the beginning and one at the end of the spectral measurement series. Sample drift was also monitored by mapping the same area again and checking the reference points on the sample. These precautions ensure that the uncertainty in the position of the measured point was minimal.

2.3. S-SNOM Imaging

s-SNOM nanoimaging based on the PsHet detection principle was performed using continuous tunable quantum cascade lasers (QCL) and an interferometric detection scheme, both integrated into the neaSCOPE instrument. This technique enables the simultaneous acquisition of the optical amplitude (IR reflectivity) and phase maps (IR absorption) at the wavelengths of interest as a function of the AFM tip position on the sample (Ocelic et al., 2006). For each Ryugu sample, a 5 μm × 5 μm area was imaged with 200 pixels × 200 pixels. The integration time was

3 ms/pixel, the AFM tip frequency was 249 kHz, the tip amplitude was 150 mV, and the tapping amplitude was ~60 nm.

2.4. Micro-FTIR Spectroscopy

Fourier transform infrared micro-spectroscopy (micro-FTIR) measurements were conducted on bulk Ryugu particles, as explained in the methods described in Kebukawa et al. (2023). IR absorption spectra were collected from each diamond window with a micro-FTIR instrument (JASCO FT/IR-6100+IRT-5200) equipped with a ceramic IR light source, a germanium-coated KBr beam splitter, a liquid-nitrogen cooled mercury-cadmium-telluride (MCT) detector, and ×16 Cassegrain mirrors. The microscope and the FTIR instruments were continuously purged with dry N_2. At each spot, 128 scans of IR transmission spectra were accumulated with a wavenumber resolution of 4 cm^{-1} and a 20 μm × 20 μm aperture. Spectra from these locations are averages of 4–20 spot measurements, which were baseline-corrected using spline curves.

2.5. Confocal Micro-Raman Spectroscopy

Raman spectroscopic measurements were conducted using a commercial confocal Raman microspectroscopy system (WITec alpha300R). This system was equipped with a 600 g/mm grating, 532 nm Nd:YAG laser, and a 50× objective (NA = 0.8). The spectrograph was calibrated using a silicon wafer substrate prior to measurements. Two-dimensional Raman intensity maps were collected with a 0.5 μm step size (pixel size), 0.1 s integration time and ~0.5 mW laser beam power on the sample surface. This corresponds to the laser power density of 5.2×10^{21} photons/cm^2, which is two orders of magnitude lower than the photodegradation threshold reported by Jakubek and Fries (2023). No systematic shift in the spectral parameters (such as peak widths or positions) was observed when multiple laser shots were directed to the same spot, indicating that these experimental parameters did not cause artificial modification of the carbonaceous matter in the samples. Raman intensity distribution maps of individual chemical components were generated by integrating the signal between the spectral endpoints of Raman peaks using a commercial software package (WITec Project). Several different profiles exist for fitting the first-order carbon bands, such as Lorentzian (Busemann et al., 2007), Voigt (Homma et al., 2015) and Lorentz-Breit-Wigner-Fano (LBWF) (Ferrari & Robertson, 2000) profiles. Our investigation of polyaromatic organic matter spectra of A0030 showed that they result in similar and comparable spectral fits (Figure S1 in Supporting Information S1). Furthermore, researchers previously fit carbon spectra with different numbers of bands due to the emergence of additional bands (D2, D3, and D4 bands, in addition to the D-band) in some data sets and the disordered carbon structures (e.g., Brunetto et al., 2009; Sadezky et al., 2005). Kouketsu et al. (2014) and Homma et al. (2015) suggested four- or five-band fitting, whereas Busemann et al. (2007) and Yesiltas, Young, and Glotch (2021) performed two-band fitting for the D and G bands. The multifunction fitting of the D- and G-bands could result in different spectral parameters; however, we did not observe a substantial difference between two-band and four-band fitting (Figure S2 in Supporting Information S1). In this work, the first-order carbon bands were fitted with two Lorentzian functions to extract the spectral parameters of the carbon bands. The spectral fitting procedure was autonomous, as opposed to manual fitting; thus, any unwanted human bias in the spectral parameters was eliminated. Fits with a coefficient of correlation (r) ≥ 0.96 were accepted, and the fits with $r < 0.96$ were discarded from the analyses.

3. Results

3.1. Nano-FTIR Spectra Within the 1,300–750 cm^{-1} (7.7–13.3 μm) Region

A total of six regions were studied within the 1,300–750 cm^{-1} (7.7–13.3 μm) spectral range, which included three regions from each of the A0030 and C0034 particles. Several spectra were collected from each region and plotted together to understand the silicate mineralogy of the Ryugu samples. Figures 1 and 2 show the nano-FTIR phase spectra of A0030 and C0034 within the 1,300–750 cm^{-1} spectral range. The spectral profiles of both samples vary substantially, which indicates that they have different silicate mineralogies. Namely, the nano-FTIR spectra of A0030 has a triplet-like profile where the peaks appear at ~945–950 cm^{-1}, ~1,030–1,040 cm^{-1}, and ~1,100–1,110 cm^{-1}, which are due to Si-O vibrations in silicates (Figure 1). A weak shoulder peak also appears in some of the spectra at ~1,070 cm^{-1}. On the other hand, the nano-FTIR spectra of C0034 present a simpler profile, with a sharp and strong peak at 1,040 cm^{-1} and a poorly resolved broad peak at 1,130–1,140 cm^{-1} (Figure 1). By comparing the IR peaks of the studied Ryugu particles with phyllosilicates from the literature (Breitenfeld

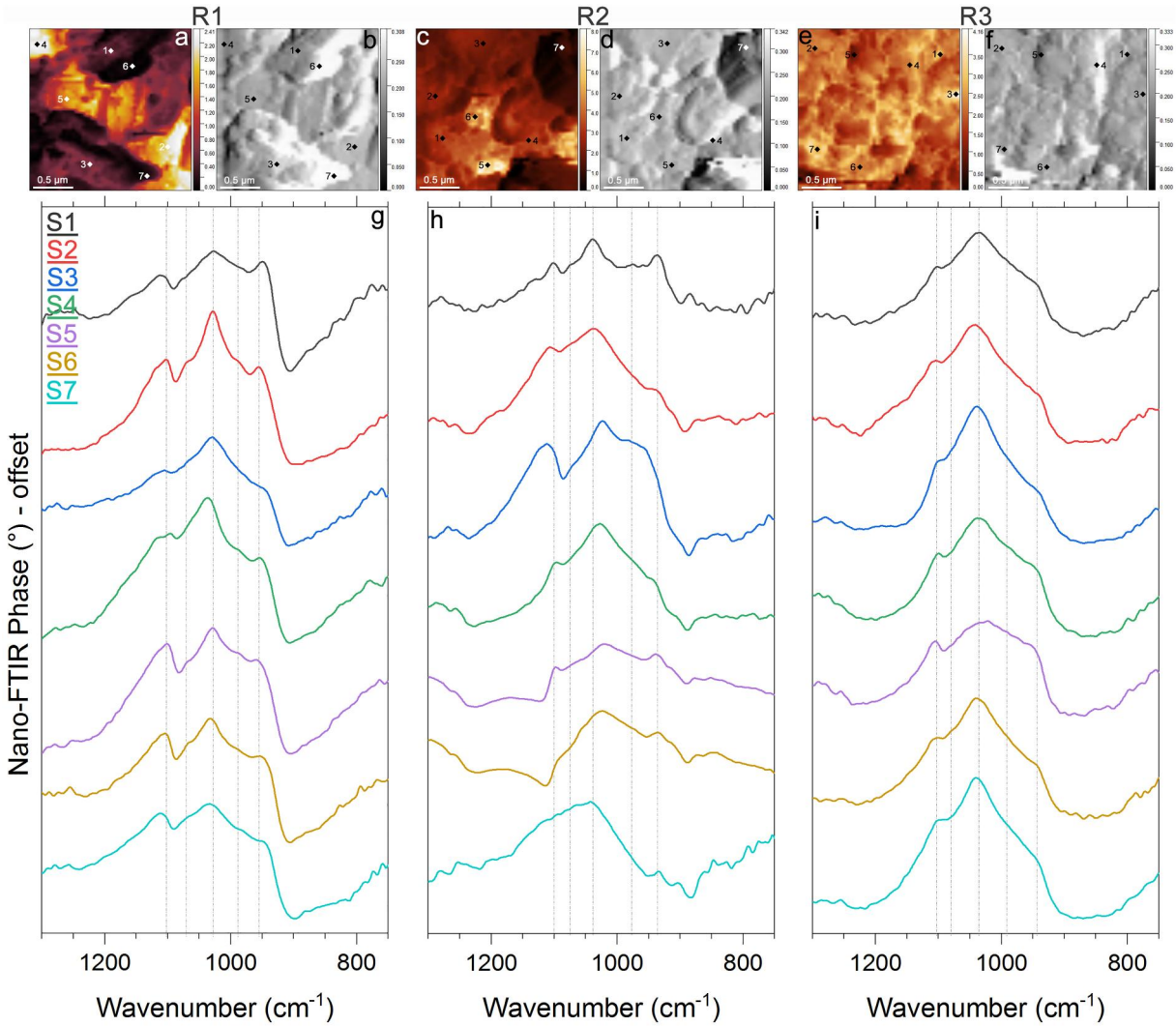

Figure 1. Near-field optical amplitude (a, c, e) and mechanical amplitude (b, d, f) images of the regions R1-R3, respectively, in A0030. Black (or white) points indicate positions of the pixels whose nano-FTIR spectra were collected. (g, h, i) Corresponding nano-FTIR spectra. Colored numbers on the top-left corner correspond to the spectra.

et al., 2021), we observe that A0030 contains serpentine-like mineralogy (i.e., mostly antigorite, with some contribution from saponite and cronstedtite), whereas C0034 contains saponite-like mineralogy (i.e., mostly saponite with some contribution from antigorite).

3.2. Nano-FTIR Spectra Within the 1,850–1,100 cm^{-1} (5.5–9.1 μm) Region

A total of 17 regions (indicated as R1, R2, and so on in the figures) were studied within the 1,850–1,100 cm^{-1} (5.5–9.1 μm) spectral range; these regions include nine from A0030 and eight from C0034. Several spectra were collected from each region (indicated as S1, S2, and so on in the figures) and plotted together to determine the organic matter, mineralogy, and water content of the Ryugu samples. The positions of the observed nano-FTIR peaks as well as their attributions are given in Table 1. Figure 3 shows the nano-FTIR spectra collected from regions R4, R5, and R6 in A0030. The spectra in R4 (Figure 3g) are characterized by peaks at 1,640 cm^{-1} (due to the OH vibrations in water) and ~1,300 cm^{-1} (due to the C-O/N-H vibrations in esters/carboxylic acids/amides). The slash sign "/" means "or" throughout the manuscript for vibrational mode assignments. S1 and S5 additionally show a very strong peaks at 1,380 cm^{-1} due to the C-H/C-O vibrations in esters/carboxylic acids/aliphatics; however, they lack the peak at 1,485 cm^{-1} due to the C = C/N − H vibrations in aromatics/amine that is present in S2–S4. The strong peak in S1 at 1,800 cm^{-1} is likely due to the C = O vibrations in lactones

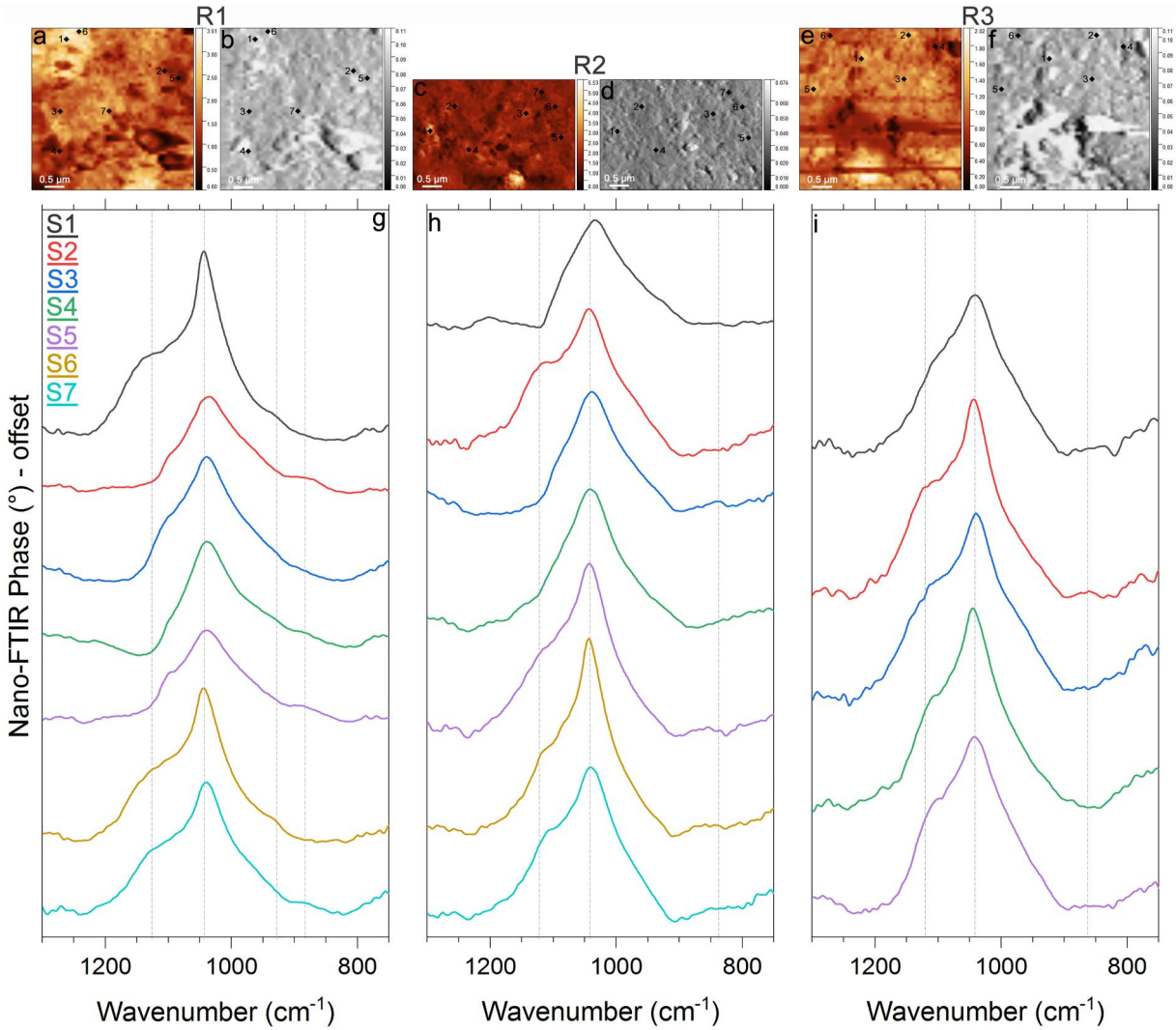

Figure 2. Near-field optical amplitude (a, c, e) and mechanical amplitude (b, d, f) images of the regions R1-R3, respectively, in C0034. Black (or white) points indicate positions of the pixels whose nano-FTIR spectra were collected. (g, h, i) Corresponding nano-FTIR spectra. Colored numbers on the top-left corner correspond to the spectra.

or carboxylic acids. Figure 3h shows the spectra collected in R5. Here, S3 and S5 contain a very strong peak at 1,351 cm^{-1} due to the C-O vibrations in esters. S1 and S2 lack this peak; however, they have a strong peak at 1,410 cm^{-1} due to the C-H/C-O vibrations in aliphatics/carboxylic acids and a weaker peak at 1,495 cm^{-1} due to the C = C/N − H vibrations in aromatics/amines. S1 additionally has a strong broad peak centered at 1,600 cm^{-1} due to the C-O/C = C/N − H vibrations in carboxylic acids/aromatics/amines. The weak peak at 1,710 cm^{-1} is present in all spectra and is due to the C-O vibrations in carboxylic acids/esters/ketones/aldehydes. The nano-FTIR spectra of R6 are shown in Figure 3i. S1 and S3 contain a broad and strong peak centered at 1,351 cm^{-1} and a very weak shoulder peak at 1,295 cm^{-1}. S3 additionally has a weak peak at 1,700 cm^{-1} due to the C=O vibrations in carboxylic acids/esters/ketones/aldehydes. The 1,295 cm^{-1} peak is the strongest in S2, which also has a broad peak centered at 1,600 cm^{-1}. S4 and S5 also have the 1,295 cm^{-1} peak, and S4 additionally shows a strong broad peak with features at 1,760 and 1,800 cm^{-1} due to C = O vibrations in lactones/carboxylic acids.

Figure 4 shows regions R7, R8, and R9 in A0030. The spectra in R7 (Figure 4g) are very similar. They all contain peaks at 1,325 cm^{-1} (due to the C-O vibrations in esters) and 1,435–1,440 cm^{-1} (due to the C-O vibrations in carbonates). S2 and S3 additionally have a weak band at 1,525 cm^{-1} due to the C=C/N-H vibrations in aromatics/amines. The 1,640 cm^{-1} peak is present in all spectra, although its intensity is very weak. S2 and S5 have a

Table 1
Position and Attribution of Observed Nano-FTIR Peaks

Position (cm^{-1})	Interpretation	Vibrational mode[a]
The 1,300-750 cm^{-1} (7.7–13.3 μm) region (silicates)		
890	Cronstedtite	Si-O
926	Antigorite	Si-O
940–950	Cronstedtite	Si-O
990	Antigorite	Si-O
1,030–1,050	Saponite, antigorite	Si-O
1,100–1,110–1,120	Antigorite	Si-O
The 1,850–1,100 cm^{-1} (5.5–9.1 μm) region (organics, carbonates, and OH)		
1,255–1,260, 1,257–1,280, 1,290–1,310	Esters, carboxylic acids, amides	C-O, N-H
1,312, 1,320, 1,326, 1,350, 1,358	Esters	C-O
1,360–1,385, 1,372	Aliphatics, esters	C-H, C-O
1,375, 1,384	Aliphatics, esters, carboxylic acids	C-H, C-O
1,410	Carbonates (calcite)	C-O
1,413, 1,425	Aliphatics, carboxylic acids	C-H, C-O
1,440	Carbonates (dolomite)	$CO3^{-2}$
1,450–1,465, 1,460–1,470	Aliphatics	C-H
1,480–1,485, 1,498–1,548, 1,507, 1,515, 1,525, 1,537	Aromatics, amines	C=C, N-H
1,556, 1,581/1,583, 1,598–1,600	Carboxylic acids, aromatics, amines	C-O, C=C, N-H
1,620	Aromatics, amine	C=C, N-H
1,640–1,660	Water	H-O-H
1,660	Amides, ketones	C=O
1,699, 1,700–1,705	Carboxylic acids, ketones, aldehydes	C=O
1,710–1,715	Carboxylic acids, esters, ketones, aldehydes	C-O
1,720–1,750	Lactones, esters, carboxylic acids, ketones	C=O
1,767	Lactones, carboxylic acids	C=O
1,800	Lactones, carboxylic acids	C=O, CO_3^{-2}

[a]possible attributions, separated by a comma.

prominent peak at 1,800 cm^{-1}. All spectra in R8 (Figure 4h) have a strong broad peak at 1,640 cm^{-1}; however, the center of this peak is at a slightly lower wavenumber (at 1,600 cm^{-1}) in S2 due to the contribution from the C-O/C = C/N-H vibrations in carboxylic acids/aromatics/amines. All spectra also have a strong peak at 1,353 cm^{-1}, and a doublet-like feature with peaks at 1,275 and 1,250 cm^{-1} due to the C-O/N-H vibrations in esters/carboxylic acids/amides. S1, S3, and S4 have a strong peak at 1,500 cm^{-1} due to the C = C/N-H vibrations in aromatics/amines. In this region, only S2 has the carbonate peak at 1,440 cm^{-1}. In R9 (Figure 4i), the 1,275 and 1,250 cm^{-1} peaks are also present in S2, but S1, S3, and S4 only have the latter peak. In contrast, S1, S3, and S4 have a broad feature at ∼1,300 cm^{-1}. S2 shows a prominent ester peak at 1,350 cm^{-1}; this peak is very weak in other spectra. S1 and S4 have a broad strong peak centered at 1,390 cm^{-1}. This peak is shifted to higher wavenumbers in S2 due to the contribution from the carbonate peak at 1,440 cm^{-1}.

Figure 5 shows regions R4-R7 in C0034. In R4, all spectra, except S6, show the peak at 1,250 cm^{-1} due to esters/carboxylic acids/amides (Figure 5i). The peak at ∼1,285 cm^{-1} is present in S4, S7, S8, and S9. S1, S2, and S5 have a strong broad peak with ester and carbonate features. S3 also has a similar broad peak; however, it is shifted to lower wavenumbers, and its features appear at 1,405 and 1,340 cm^{-1}. Spectra S4 and S7–S9 don't contain this peak; instead, they have a broad peak centered at ∼1,480 cm^{-1}. In R5, all spectra, except S6, have a prominent peak at 1,350 cm^{-1}. S1–S4, S6–S7, and S9 show a carbonate peak at 1,440 cm^{-1} (Figure 5j). Those that lack the

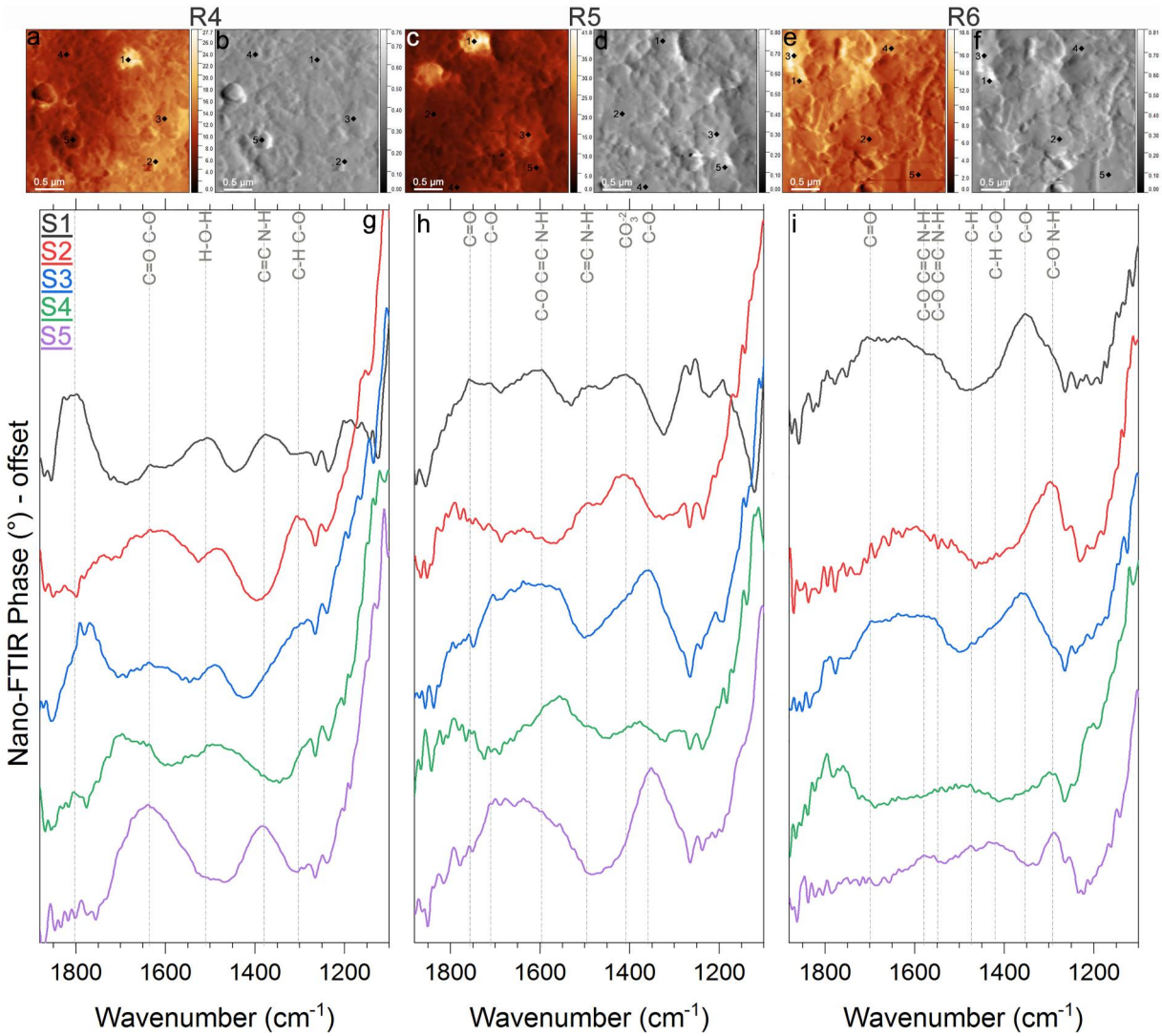

Figure 3. Near-field optical amplitude (a, c, e) and mechanical amplitude (b, d, f) images of the regions R4-R6, respectively, in A0030. Black (or white) points indicate positions of the pixels whose nano-FTIR spectra were collected. (g, h, i) Corresponding nano-FTIR spectra. Colored numbers on the top-left corner correspond to the spectra.

carbonate peak have a sharp peak at 1,470–1,475 cm^{-1} due to aliphatics. All spectra, except S6 and S9, have a peak at 1,525–1,535 cm^{-1}. S6 and S9 lack this peak; however, they have a peak at 1,505 cm^{-1} that is also due to aromatics/amines. In addition, the 1,600 cm^{-1} peak is present only in S6 and S9. This result potentially indicates the presence of different aromatics/amines in this region. In R6, S1 and S3 have a sharp peak at 1,290 cm^{-1} and at 1,358 cm^{-1}; however, all other spectra lack these peaks (Figure 5k). S2 has features at 1,340 and 1,440 cm^{-1}; however, the other spectra don't have these features. A strong peak appears at 1,540 cm^{-1} in all spectra except S2. Various sharp features are observed in the nano-FTIR spectra collected in R7 (Figure 5l). The most prominent peak is at 1,485 cm^{-1}. Other features appear at 1,290 cm^{-1} and 1,340–1,325 cm^{-1}.

Figure 6 presents regions R8-R11 in C0034. The nano-FTIR spectra in R8 have sharp ester features at 1,312 and 1,360 cm^{-1}. Aliphatic/carboxylic acid feature at 1,414 cm^{-1} is present only in S4). S2 and S3 have aliphatic features at 1,455 and 1,475 cm^{-1} (Figure 6i). S1 and S4 additionally have a strong peak at 1,550 cm^{-1} due to the C-O/C = C/N-H vibrations in carboxylic acids/aromatics/amines. All spectra in R9 have a peak at 1,345 cm^{-1} (Figure 6j). S1 and S3 present a carbonate peak at 1,440 cm^{-1}; however, S2 lacks this peak. Instead, S2 has a very strong and sharp peak centered at 1,517 cm^{-1} due to aromatics/amines, whereas this peak is much weaker in S1 and S3. R10 has several spectra with a prominent peak at 1,290 cm^{-1} (Figure 6k). This peak is absent in S2 and

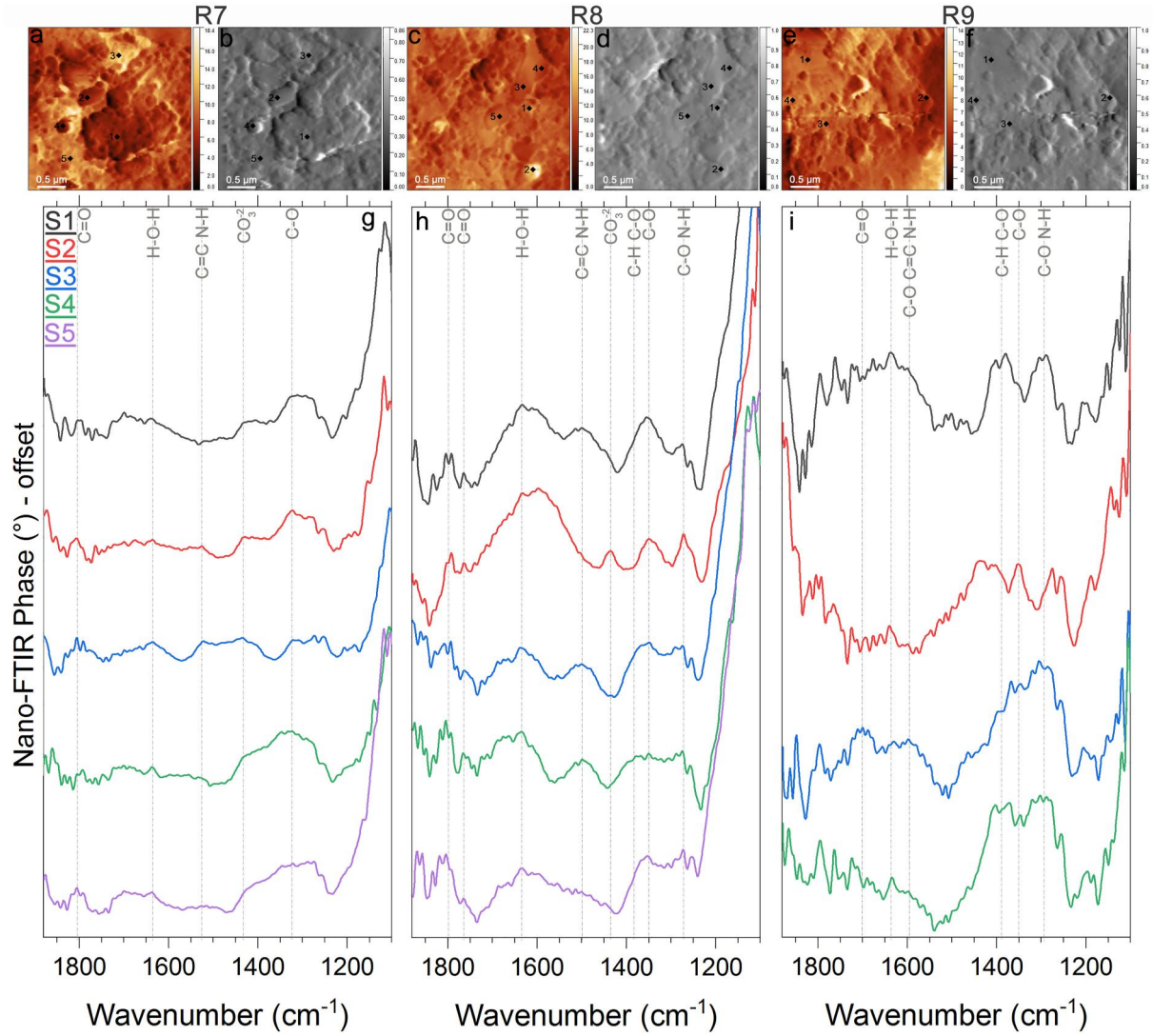

Figure 4. Near-field optical amplitude (a, c, e) and mechanical amplitude (b, d, f) images of the regions R7-R9, respectively, in A0030. Black (or white) points indicate positions of the pixels whose nano-FTIR spectra were collected. (g, h, i) Corresponding nano-FTIR spectra. Colored numbers on the top-left corner correspond to the spectra.

S6; S2 and S6 instead have a broad peak centered at ~1,350 cm^{-1}. Spectra S3–S5 show a broad peak at approximately 1,470 cm^{-1} that is likely a combination of two features at 1,485 and 1,440 cm^{-1}. S2 has a broad peak centered at ~1,525 cm^{-1}; this peak is absent in the other spectra. Last, in R11, S2–S4 has a prominent broad peak at 1,300 cm^{-1} (Figure 6l). A sharp feature at 1,385 cm^{-1} due to esters/carboxylic acids/aliphatics is present in all spectra. This feature is accompanied by the peak at 1,425 cm^{-1} due to aliphatics/carboxylic acids in S1 and S5. S1 has the 1,600 cm^{-1} peak and lacks the water peak at 1,640 cm^{-1}. This peak is present in S3–S5.

A small fragment from the A0030 particle was prepared as an S-embedded and ultramicrotomed mount and studied within the 1,850–1,100 cm^{-1} (5.5–9.1 μm) region. A total of three regions (R10, R11, and R12) were investigated via nano-FTIR. The nano-FTIR spectra collected in R10 appear similar to each other because most of the nano-FTIR spectra were collected from the same phase (Figures 7a and 7b). A triplet with peaks at 1,320, 1,284, and 1,256 cm^{-1} is observed in most spectra; spectra were collected from the same region on the sample (see Figures 7a and 7b). All spectra also show the carbonate band. This particular particle also shows a strong and broad peak centered at 1,615–1,620 cm^{-1} due to aromatics/amines. The nano-FTIR spectra collected in R11 are similar to those in R10; they show the triplet, the carbonate peak, and the aromatic/amine peak at 1,615–1,620 cm^{-1}. In addition, most spectra in R11 have peaks at 1,382 and 1,485 cm^{-1}. In the nano-FTIR spectra

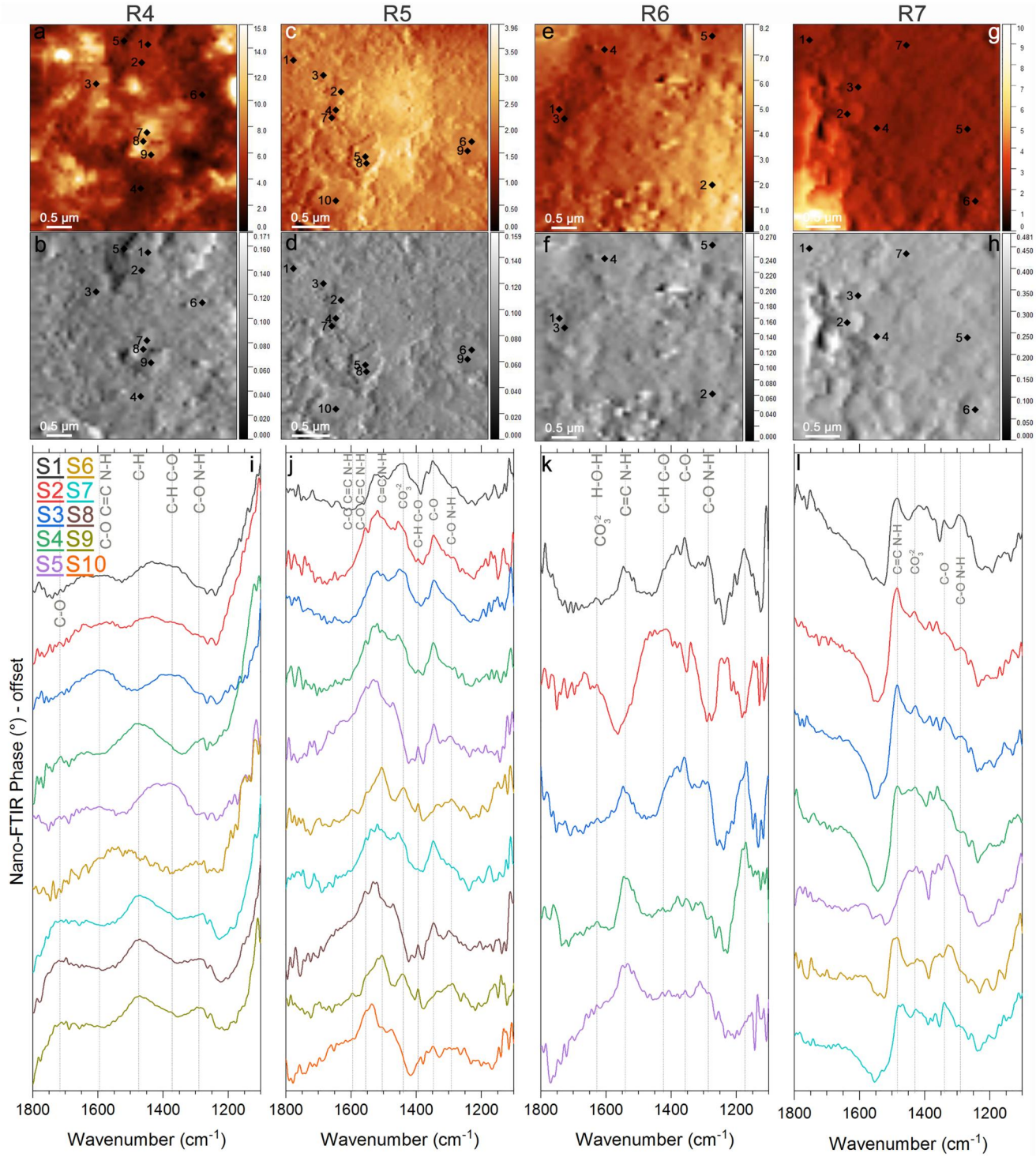

Figure 5. Near-field optical amplitude (a, c, e, g) and mechanical amplitude (b, d, f, h) images of the regions R4-R7, respectively, in C0034. Black (or white) points indicate positions of the pixels whose nano-FTIR spectra were collected. (i, j, k, l) Corresponding nano-FTIR spectra. Colored numbers on the top-left corner correspond to the spectra.

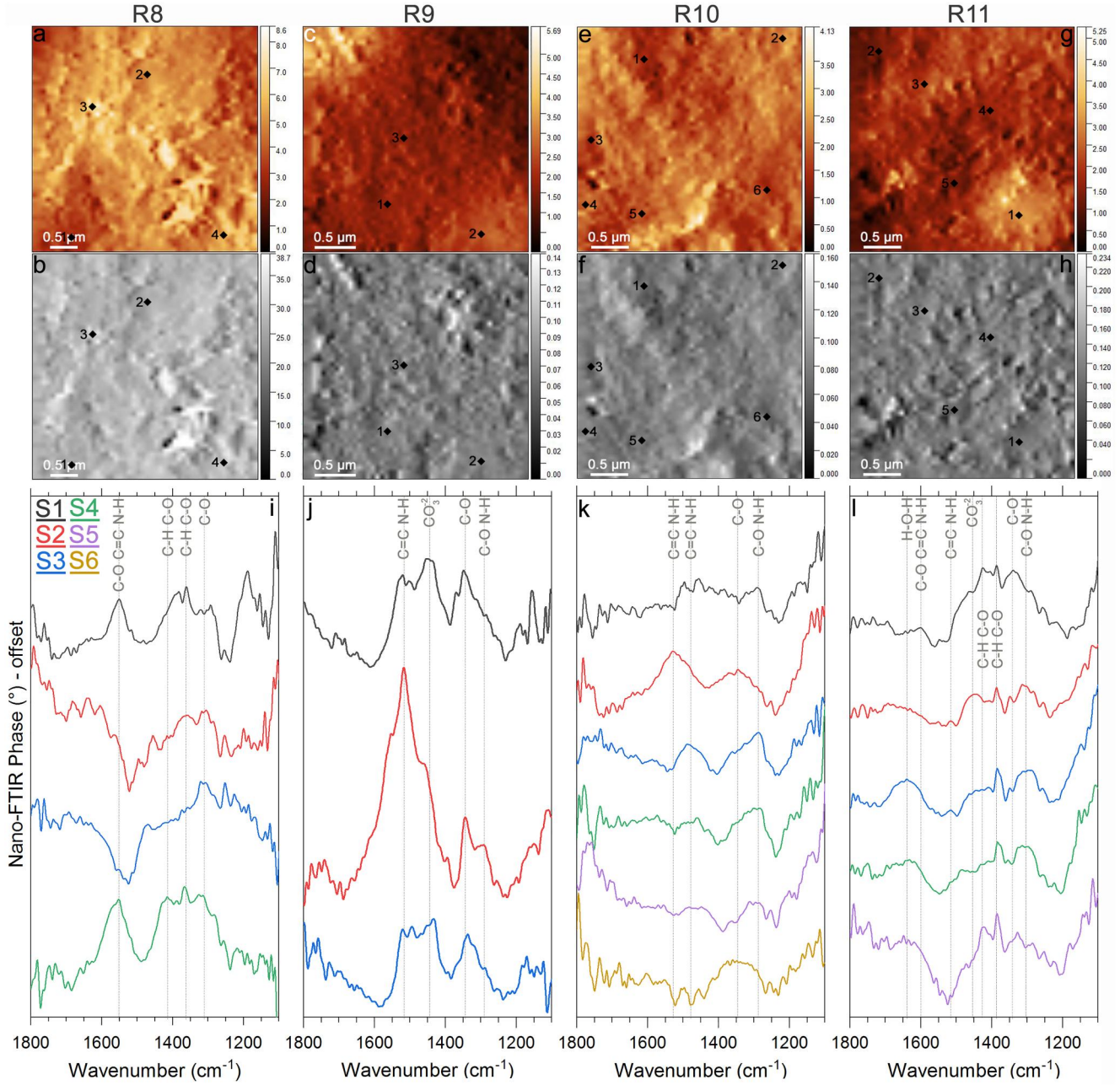

Figure 6. Near-field optical amplitude (a, c, e, g) and mechanical amplitude (b, d, f, h) images of the regions R8-R11, respectively, in C0034. Black (or white) points indicate positions of the pixels whose nano-FTIR spectra were collected. (i, j, k, l) Corresponding nano-FTIR spectra. Colored numbers on the top-left corner correspond to the spectra.

collected from R12, the most prominent peak appears at 1,385 cm^{-1}. Most spectra also have a peak near 1,485 cm^{-1} and a broad water peak near 1,635–1,630 cm^{-1}.

3.3. Nanoscale Optical Phase Mapping

We collected nanoscale SNOM-based phase maps on both Ryugu samples to determine the locations of various chemical components in the samples (Figure 8). The first two images in each row show the topography (height) and optical amplitude (IR reflectivity) maps of the two samples, and are followed by the optical phase (IR absorption) maps for 1,040 cm^{-1} (phyllosilicates), 1,250 cm^{-1} (esters/carboxylic acids/amides), 1,325 cm^{-1}

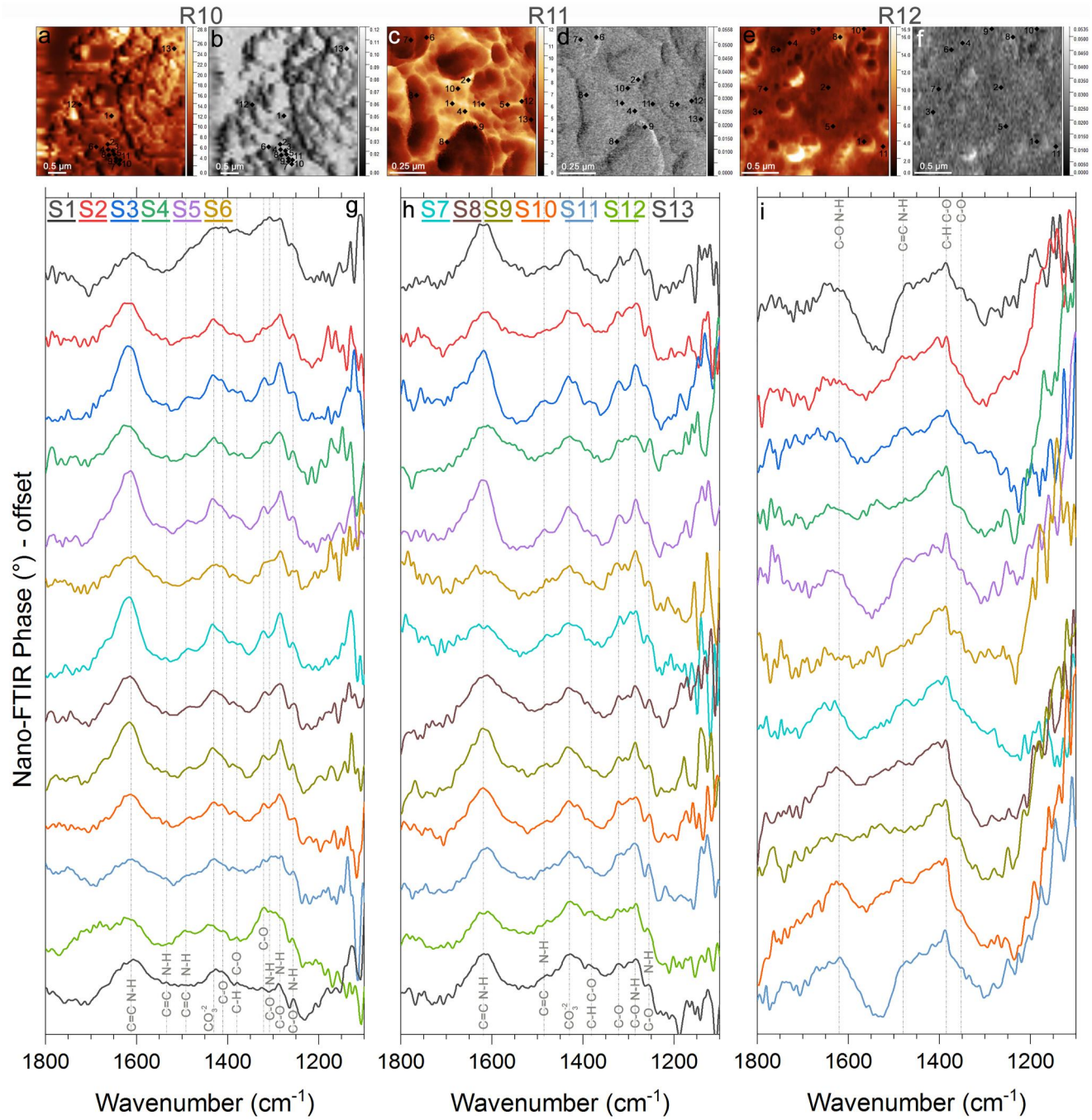

Figure 7. Near-field optical amplitude (a, c, e) and mechanical amplitude (b, d, f) images of the regions R10-R12, respectively, in the sulfur-embedded A0030 particle. Black (or white) points indicate positions of the pixels whose nano-FTIR spectra were collected. (g, h, i) Corresponding nano-FTIR spectra. Colored numbers on the top-left corner correspond to the spectra.

(esters), 1,440 cm^{-1} (carbonates), and 1,600 cm^{-1} (carboxylic acids/aromatics/amines) for the A0030 (top row, Figures 8c–8g) and C0034 fragments (bottom row, Figures 8j–8n). The phase maps show that both samples contain abundant phyllosilicates, and they show no correlation with other components (Figure 9). For A0034 (blue tiles in Figure 9), (a) the 1,250 cm^{-1} map is negatively correlated with both the 1,325 cm^{-1} ($r = -0.70$) and 1,600 cm^{-1} ($r = -0.60$) maps, and (b) the 1,325 and 1,600 cm^{-1} maps are positively correlated ($r = 0.73$). The 1,440 and 1,600 cm^{-1} maps have zero correlation ($r = 0.01$). If the 1,600 cm^{-1} map had any contribution from water, it would show a correlation greater than 0.01. For C0034 (red tiles in Figure 9), (a) the 1,250 cm^{-1} map is

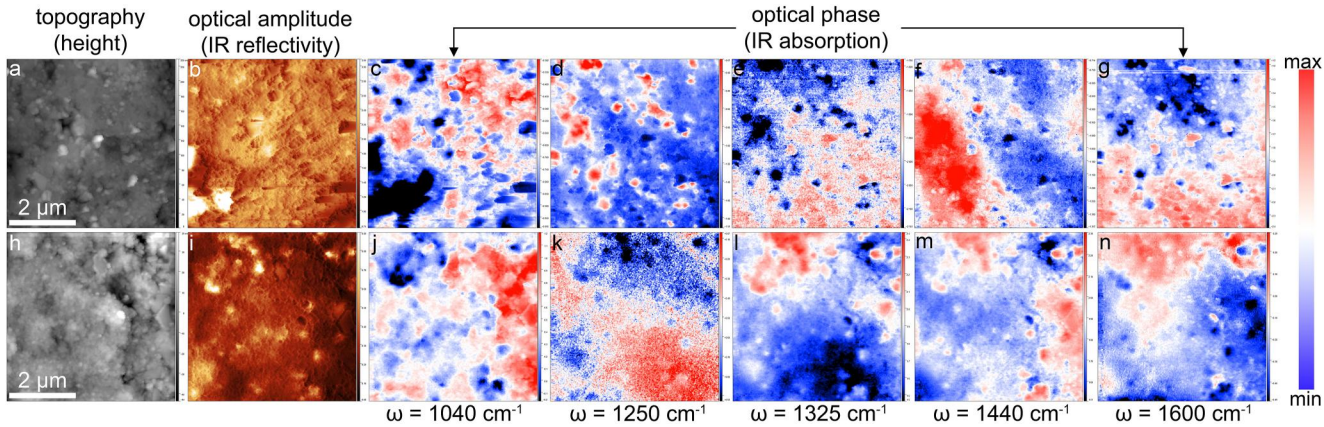

Figure 8. Topography, optical amplitude, and optical phase maps of A0030 (top panel) and C0034 (bottom panel) based on PsHet detection.

negatively correlated with the 1,325 cm^{-1} map ($r = -0.50$) but is not correlated with the 1,600 cm^{-1} map, and (b) the 1,325 and 1,600 cm^{-1} maps are very weakly positively correlated ($r = 0.31$). Figure 10 presents the false-color composite phase images to show the relative distributions of the identified chemical compounds. The red component in Figures 10a,c,d,f represents the distribution of the 1,040 cm^{-1} peak due to phyllosilicates and is the major component in the studied regions. The 1,250 cm^{-1} component (the C-O/N-H vibrations in esters/carboxylic acids/amides) is present as discrete grains in A0030, whereas it is present as a diffused component in C0034 (red component in Figures 10b and 10e). Conversely, the opposite is true for the 1,325 cm^{-1} component (the C-O vibrations in esters). This component is present as a diffused material in A0030 but as discrete grains in C0034.

3.4. Micro-Raman Spectroscopy and Imaging

Micro-Raman analyses demonstrate that the A0030 and C0034 particles contain abundant polyaromatic organic matter. As shown in Figure 11, the micro-Raman map of a region on A0030 (red square) shows that this sample contains polyaromatic OM, chromite, and anhydrous silicates olivine and pyroxene. The polyaromatic OM, whose spectrum shows first-order carbon bands (Figure 11c, blue), appears to be distributed in large domains as well as in web-like structures surrounding pyroxene and chromite. The chromite spectrum (Figure 11c, red) shows a single peak at 661 cm^{-1}. The olivine spectrum (Figure 11c, green) has a characteristic doublet with peaks at 835 and 853 cm^{-1}. The pyroxene spectrum (Figure 11c, yellow) contains a doublet with peaks at 1,014 and 1,031 cm^{-1}, another doublet with peaks at 664 and 687 cm^{-1}, and a single peak at 340 cm^{-1}. The micro-Raman map of an S-embedded C0034 fragment also shows magnetite, hematite, sulfide, and abundant polyaromatic OM (Figure 12). The lower part of the C0034 fragment was out of focus due to topographic variations in the sample; thus, the micro-Raman data of this part were not usable and appeared as black in Figure 12b.

The first-order carbon peaks of polyaromatic OM appear at ~1,364 cm^{-1} (the D band, due to sp^3 carbon bonding and the breathing motion of sp^3 atoms in rings) and 1,592 cm^{-1} (the G band, due to stretching mode of sp^2 atoms in polyaromatic rings) (Ferrari & Robertson, 2000; Starkey et al., 2013; Suzuki et al., 2010; Tuinstra & Koenig, 1970). The exact values of the spectral parameters of these peaks (their positions (ω), full-width-half-maxima (Γ), and amplitudes (I)) are modified as a result of thermal metamorphism because their structures are sensitive to heating, and elevated temperatures cause them to be more graphitic and increase their aromaticity (Beyssac et al., 2002; Ferrari & Robertson, 2000; Sadezky et al., 2005; Tuinstra & Koenig, 1970). As such, the thermal metamorphic history of primitive extraterrestrial materials and its extent in the parent body can be inferred from the spectral characterization of polyaromatic OM. Specifically, spectral properties of first-order carbon D and G bands can be quantitatively studied and compared to assess the maturation grade, extent of polymerization and aromatization, and ultimately thermal metamorphic history of a given sample (e.g., Beyssac et al., 2002; Busemann et al., 2007; Cody et al., 2008; Schmidt & Hinrichs, 2020; Starkey et al., 2013; Visser et al., 2018; Yesiltas, Young, & Glotch, 2021). We studied ~500 Raman spectra from each Ryugu particle and compared their spectral parameters to determine the thermal metamorphic history of the parent asteroid. Figures 13a and 13b presents the extracted and average polyaromatic OM Raman spectra. Figure 13c

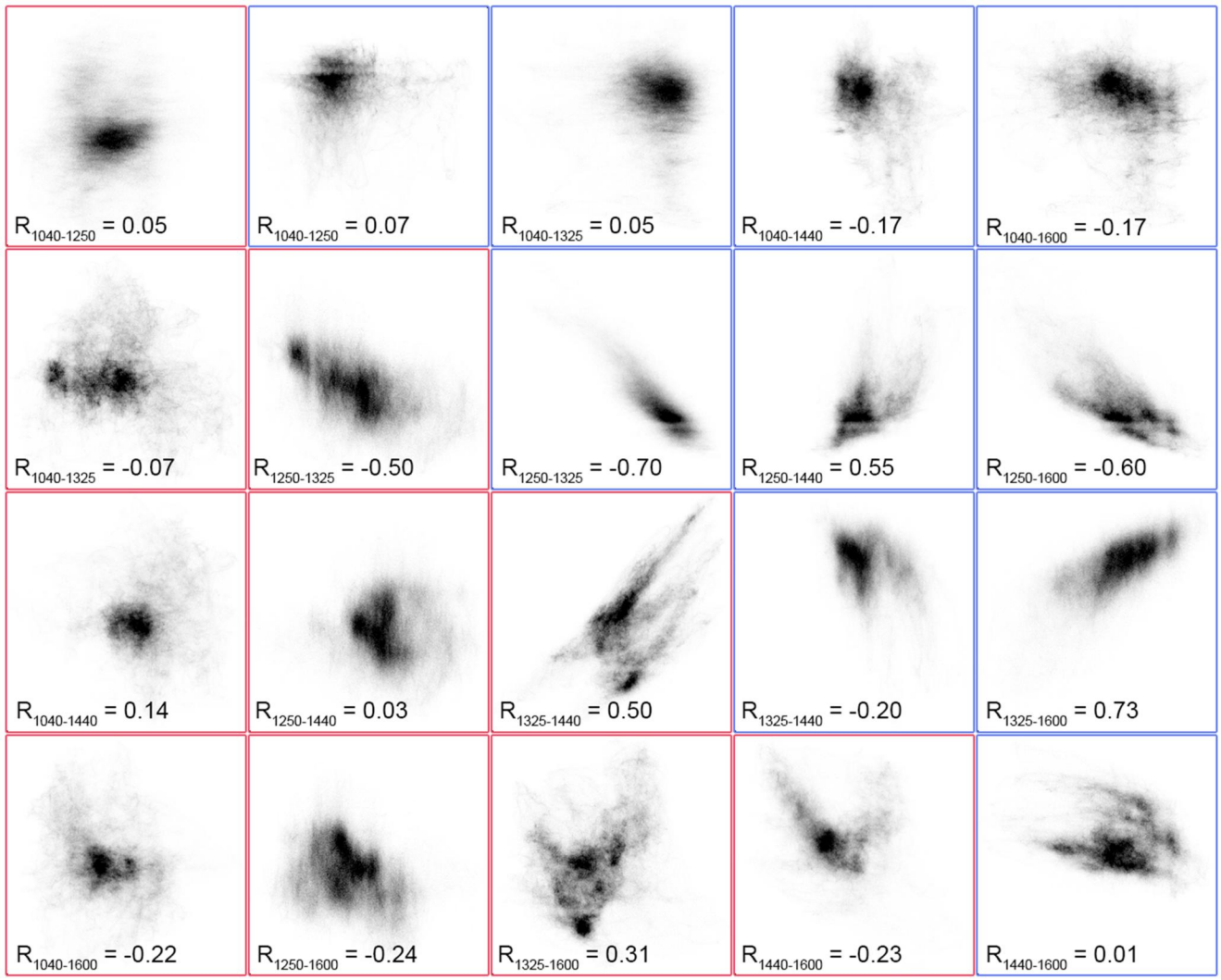

Figure 9. Statistical correlation coefficients of the five chemical components (shown in Figure 8) for A0030 (blue tiles) and C0034 (red tiles).

shows that the position of the G band increases with increased thermal metamorphism; additionally, C0034 plots near the petrologic type-1 carbonaceous chondrite Orgueil, whereas A0030 plots near petrologic type-2 carbonaceous chondrites (the average of CM2 and CR2 chondrites). Petrologic type-3 carbonaceous chondrites have even higher ω_G, indicating higher thermal metamorphism, that is, elevated temperatures in the parent asteroid (the CO3 and CV3 Raman data are from Yesiltas, Young, and Glotch (2021)). Figure 13d compares the Γ and ω of the G band; an increase in the thermal metamorphism results in a lower Γ_G and higher ω_G. Here, C0034 again appears very close to the type-1 carbonaceous chondrite Orgueil, and A0030 appears further lower in this domain. The peak metamorphic temperature (PMT) of the parent asteroids can be roughly estimated using the Raman spectral parameters of the D or G bands (e.g., Beyssac et al., 2002; Busemann et al., 2007; Cody et al., 2008; Schmidt & Hinrichs, 2020; Visser et al., 2018). The Raman carbon thermometry models introduced by these groups are generally applicable to higher temperature carbonaceous materials (>200°C). Because the model by Schmidt and Hinrichs (2020) (based on Γ_G) is currently more appropriate for lower petrologic type carbonaceous chondrites (types 1 and 2), we used their model and calculated the PMT of the Ryugu samples as well as the carbonaceous chondrites (Figure 13e). The PMTs of C0034 and A0030 were calculated to be ~75.15 ± 14.05°C and ~93.81 ± 12.88°C, respectively.

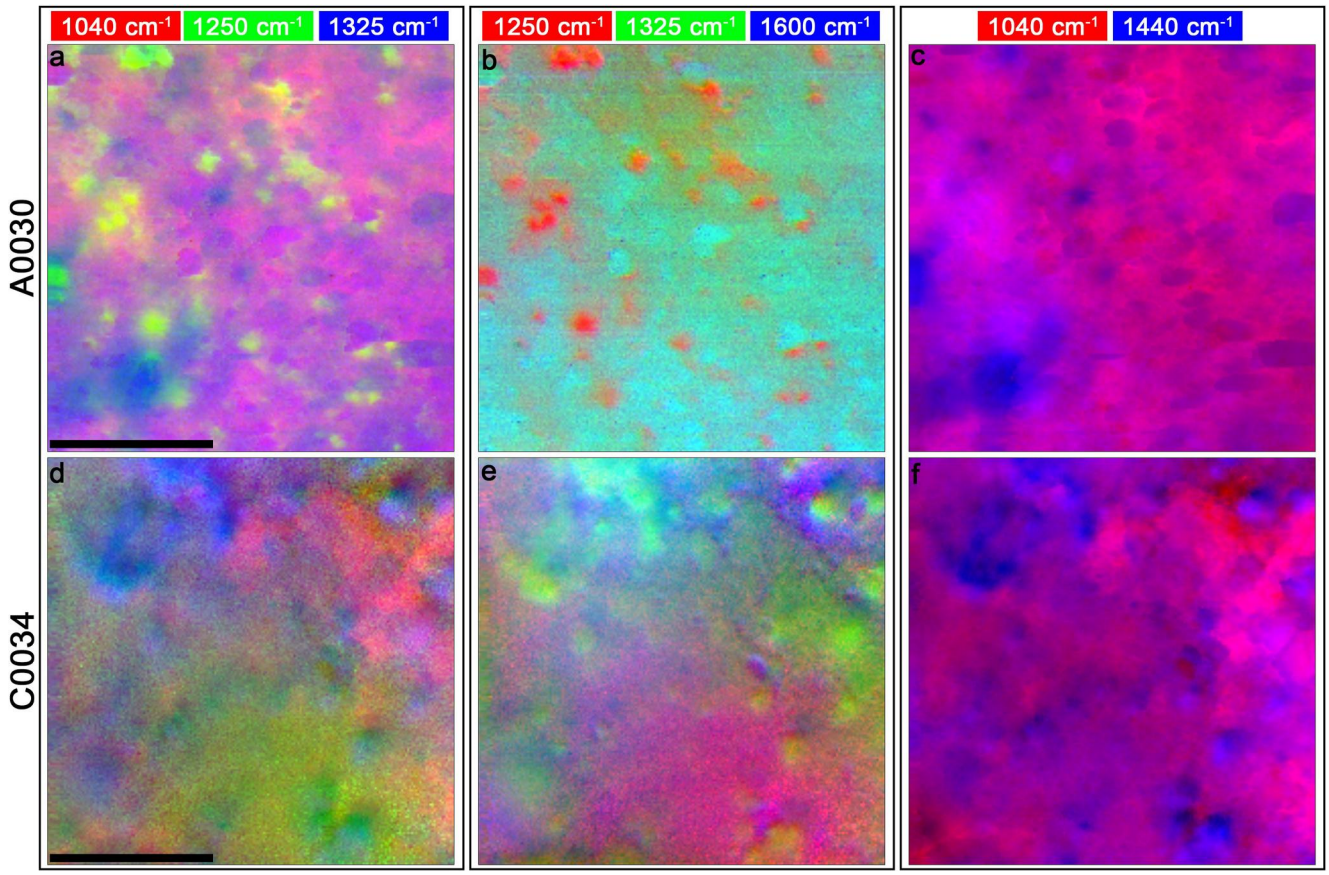

Figure 10. False-color composite phase maps of A0030 (top panel) and C0034 (bottom panel). Each color, whose vibration frequency is given above the maps, represents different molecular composition in the Ryugu particles. Black scale bar is 2 μm.

4. Discussion

4.1. Parent Body Processes

The presence of phyllosilicates and carbonates indicates extensive and heterogeneous aqueous alteration (Ito et al., 2022; Nakamura, Matsumoto, et al., 2022; Yokoyama et al., 2022). Our nanoscale IR spectroscopic and microscopic investigation is in good agreement with the previous observations. We also observed that the aqueous alteration was incomplete, as indicated by the presence of anhydrous silicates, such as olivine and pyroxene, in the studied Ryugu particles. This observation, together with the absence of chondrules in the Ryugu particles, may also indicate that olivine and/or pyroxene could be exogeneous, as has been seen in remote sensing data of Bennu (DellaGiustina et al., 2021; Hamilton et al., 2021). The silicate mineralogy of Ryugu particles A0030 and C0034 differs from each other. A0030 contains more serpentine-like mineralogy, whereas C0034 contains more saponite-like mineralogy. Differences in aqueous geochemistry, alteration temperature, pH, conditions, and/or original primary mineralogy could be responsible for heterogeneous silicate mineralogy. Another possibility could be incomplete and/or heterogeneous aqueous alteration, which could result in heterogeneous silicate mineralogy, such as those observed in the studied Ryugu particles. Whether surface processes (solar wind, heating, and impacts) play any role in the observed differences in the silicate mineralogy of Ryugu particles is currently unknown.

The absence of highly graphitic carbonaceous material in the Ryugu particles indicates that Ryugu did not experience elevated temperatures. The PMT of the studied Ryugu particles are <100°C, which is consistent with other Ryugu particles (e.g., Yokoyama et al., 2022). Moreover, A0030 has a slightly higher PMT than C0034. In addition to the observed compositional differences in the organic matter content of the Ryugu particles, their distribution varies as well. The organic matter is distributed as discrete nanoscale organic grains as well as

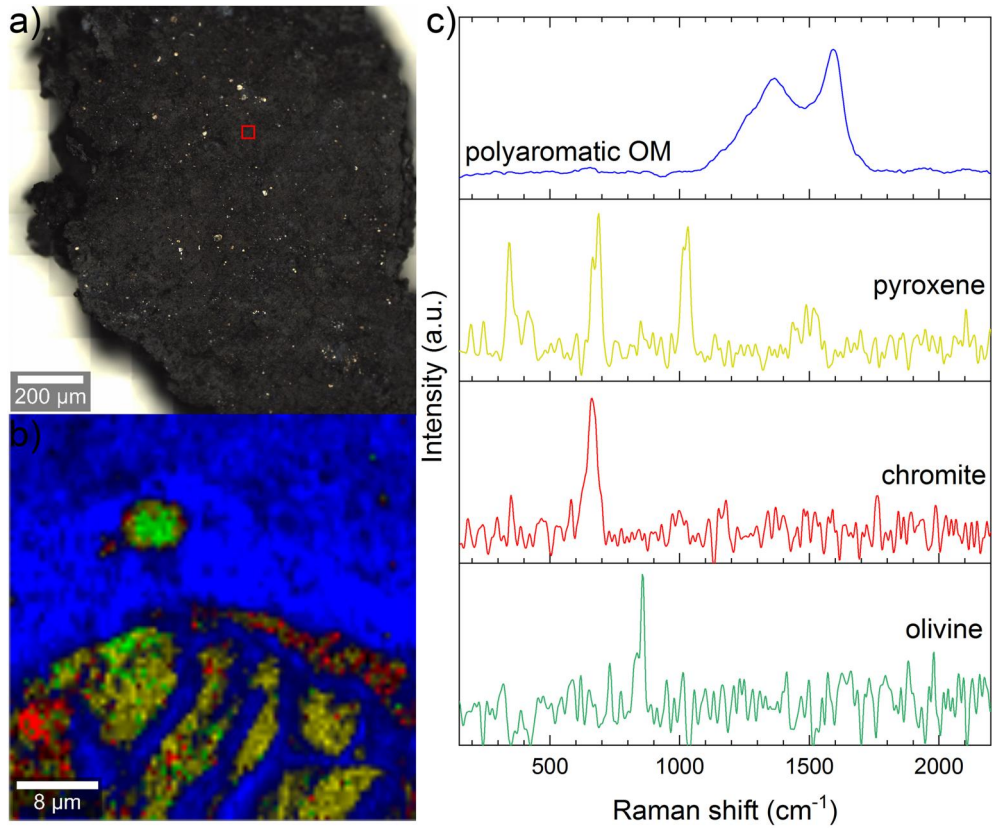

Figure 11. 2D micro-Raman mapping of a region in A0030. (a) visible light image of the sample. Red square indicates the mapped area. (b) Compositional distribution of the observed components. Blue: polyaromatic OM, yellow: pyroxene, red: chromite, green: olivine. (c) Corresponding color-coded micro-Raman spectra.

dispersed materials in the matrix of the studied Ryugu grains. These differences could be in part due to surface processes, such as space weathering on Ryugu, from which the subsurface particles mostly escape. The differences in the organic matter also likely reflect the inherent heterogeneity of the organic matter in Ryugu's parent asteroid.

4.2. Spectral Characteristics

The conventional micro-FTIR spectra of Ryugu particles A0030 and C0034 show IR peaks and features due to OH in phyllosilicates, adsorbed/interlayer water, aliphatic hydrocarbons, aromatics and/or interlayer water, carbonates, and phyllosilicates (Figure 14). These IR absorption features are consistent with Yabuta et al. (2023), Dartois et al. (2023), and Kebukawa et al. (2023). These IR spectra represent average compositions of typically a few tens of microns. In contrast, the nano-FTIR spectra show much greater diversity in the spectral components, reflecting the local nanoscale heterogeneity of the phyllosilicate composition. At 1,030–1,050 cm^{-1}, there is always a large peak attributed to phyllosilicates, such as saponite and serpentine minerals. Some additional peaks or shoulders often appear at ∼950 cm^{-1} and/or ∼1,100 cm^{-1} due to potential contributions from serpentine minerals, such as chrysotile, lizardite, antigorite, and cronstedtite (Breitenfeld et al., 2021; Salisbury et al., 1991). These peaks are more distinct in A0030 than in C0034, indicating a larger fraction of serpentine minerals in the A0034 sample. Saponite and serpentine in the Ryugu particles often appear as serpentinite–saponite intergrowth, which could not be distinguished even with nano-FTIR with ∼20 nm spatial resolution. It is also worth mentioning the lack of detection of phyllosilicates in our Raman spectroscopic results, which are difficult to detect with Raman spectroscopy. This further demonstrates that nano-FTIR spectroscopy is one of the most suitable non-destructive techniques for the investigation of primitive extraterrestrial materials, such as returned samples like Ryugu and Bennu.

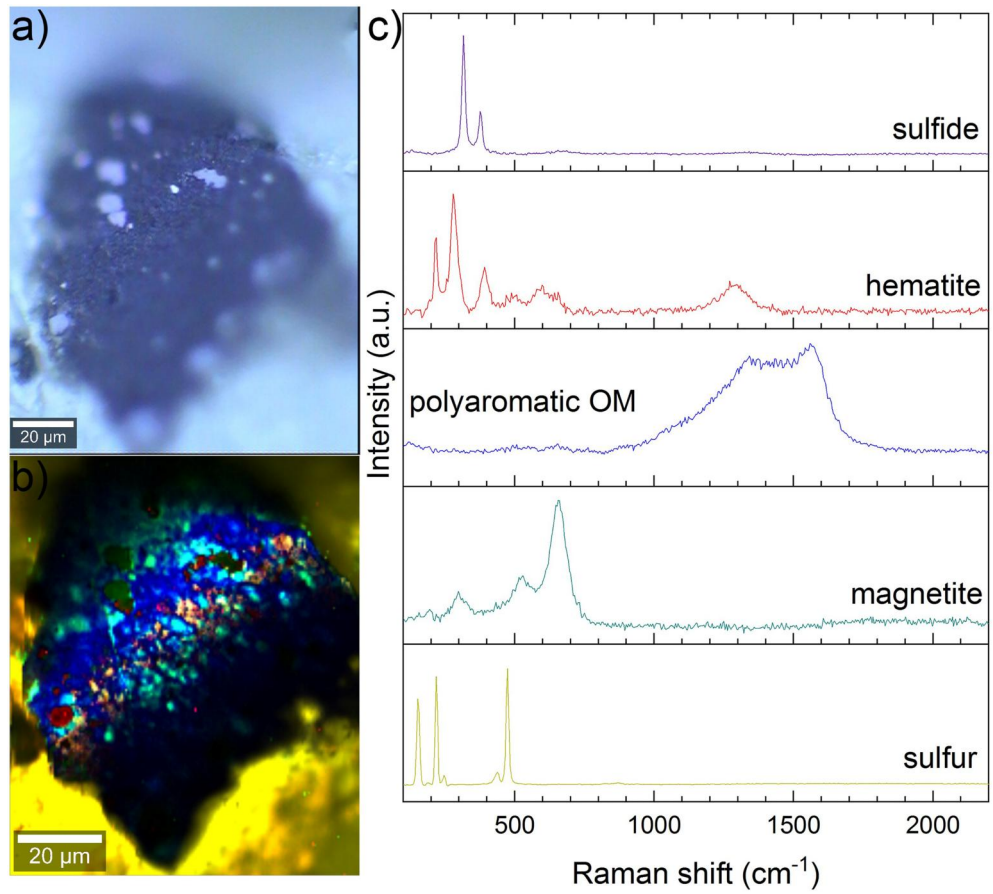

Figure 12. 2D micro-Raman mapping of a region in C0034. (a) visible light image of the sample. (b) Compositional distribution of the observed components. Purple: sulfide, red: hematite, blue: polyaromatic OM, green: magnetite, yellow: sulfur. (c) Corresponding color-coded micro-Raman spectra.

In general, the acid residues of Ryugu samples are similar to the insoluble organic matter (IOM) of the unheated carbonaceous chondrites (CI, CM, and CR) (Kebukawa et al., 2023-a); the characteristic C = O and aromatic C = C peaks at ~1,700 and ~1,600 cm^{-1}, respectively, smaller aliphatic C-H peaks at ~1,450 and ~1,375 cm^{-1}, a broad C-O and the aromatic skeletal peak at ~1,230 cm^{-1}, and the aliphatic C-H peaks at ~2,900 cm^{-1} are present. However, there are some differences between Ryugu residues and chondrite IOM; Ryugu residues have a peak at 1,660 cm^{-1} that could be potentially attributed to C = O from the unsaturated ketones/aldehydes or amides (Kebukawa et al., 2023; Yabuta et al., 2023). In addition, two minor "outlier phases" were found in the Ryugu acid residues (Kebukawa et al., 2023-a). One has characteristic IR peaks at 1,660 and 1,635 cm^{-1}, which are potentially from primary amide-like compounds, and the other has characteristic IR peaks at 1,510, 1,245, 1,180, 1,040, and 830 cm^{-1}, likely due to unknown aromatic-carbonyl-ether compounds (Kebukawa et al., 2023-a).

The nano-FTIR spectra of Ryugu A0030 and C0034 does not exactly match any of the above. Some spectra show a possible aromatic C = C peak near 1,600 cm^{-1}, but the ~1,700 cm^{-1} (C=O) peak is either not coupled with the ~1,600 cm^{-1} peak or not well distinguished, with the exception of one spectrum shown in Figure 4i (spectrum 3). The 1,700 cm^{-1} peak is common in A0030 but not clear in C0034. Ryugu samples from chamber C could contain impact ejecta from subsurface materials, and therefore perhaps the C0034 sample was affected by the impact. Alternatively, the lack of the 1,700 cm^{-1} peak in C0034 might also be due to the heterogeneous composition of the Ryugu samples. Particle-to-particle heterogeneity is commonly observed in Ryugu samples in terms of both organics (Dartois et al., 2023; Kebukawa et al., 2023-a; Yabuta et al., 2023) and minerals (Ito et al., 2022; Nakamura, Matsumoto, et al., 2022; Yokoyama et al., 2022). Therefore, we favor the particle-to-particle heterogeneity of the Ryugu samples rather than the impact-induced C=O loss.

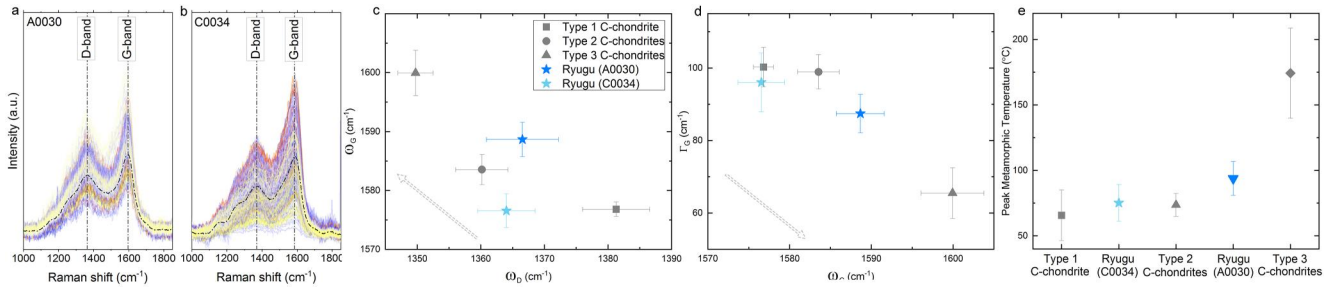

Figure 13. (a, b) Micro-Raman spectra of polyaromatic OM observed in A0030 and C0034. Dashed black curves represent average spectra. Vertical dashed lines indicate positions of the D and G first-order carbon bands. (c, d) Comparision of the Raman spectral parameters and (e) Estimated peak metamorphic temperatures for both Ryugu particles and carbonaceous chondrites. PMT values for type-3 chondrites are from Yesiltas, Young, and Glotch (2021), recalculated using the equation in Schmidt and Hinrichs (2020). The dashed gray arrows indicate increasing thermal metamorphism.

In the nano-FTIR spectra, notable peaks are often observed near 1,800 cm^{-1}, 1,550–1,500 cm^{-1}, and 1,400-1,300 cm^{-1}. The peak at 1,800 cm^{-1} could be C=O in lactones and/or carboxylic acids, the 1,550–1,500 cm^{-1} peak could be aromatic C=C and/or N-H in amines, and the 1,400–1,300 cm^{-1} peak could be C-O and/or aliphatic C-H. Because of the overlapping IR characteristic peak positions of some functional groups, the 1,550-1,500 cm^{-1} peak could be attributed to both aromatic C=C and amine N-H, and the presence of N-containing functional groups from these spectra was difficult to discern. The characteristic IR features of the amide-like outlier phase (Kebukawa et al., 2023-a) are not observed in the nano-FTIR spectra; however, in the case of the amide-like outlier phase, the possibility that the HF/HCl treatment altered the N-bearing functional groups could not be ruled out since amide structures are susceptible to acid hydrolysis. In any case, there are large nanoscale variations in the functional groups of the studied Ryugu particles, indicating that aqueous alteration in the Ryugu parent body did not result in homogeneous composition. This is potentially because the organics were either insoluble in water and/or strongly adsorbed on the minerals. The local heterogeneity of minerals, which might be the result of heterogeneous aqueous alteration processes, composition and/or pH of the alteration fluid,

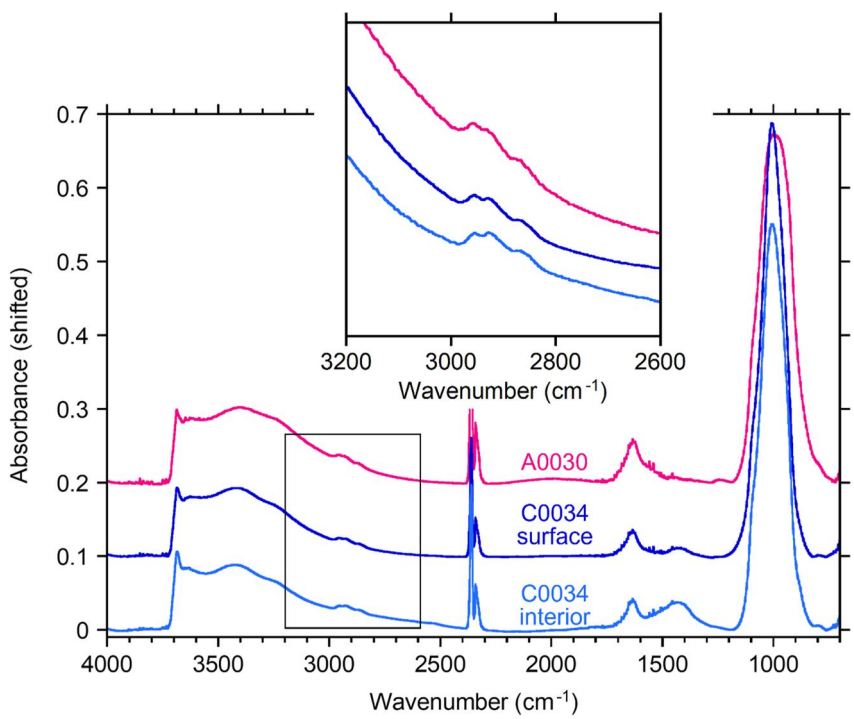

Figure 14. Micro-FTIR spectra of A0030 and C0034 particles within the mid-IR spectral range. The inset shows the aliphatic C-H region indicated by the black rectangle.

space weathering, or impacts, could also result in different compositions of organics (Hirakawa et al., 2021; Viennet et al., 2022; Vinogradoff et al., 2020).

4.3. Spatial Distributions

In the nano-FTIR phase maps (Figure 8), a strong correlation is observed between 1,600 cm^{-1} and 1,325 cm^{-1} (see Figure 9 for correlation coefficients), indicating that these absorptions are due to organics with C=C and C-O functional groups, probably in macromolecular OM. The OM distribution is mostly distinguished from phyllosilicates (1,040 cm^{-1}) and carbonates (1,440 cm^{-1}), which is inconsistent with previous FTIR results that show overlapping organics and phyllosilicates (and carbonates, in some cases) (Kebukawa et al., 2010, 2019; Yesiltas et al., 2015; Yesiltas & Kebukawa, 2016). However, this is reasonable given the much higher spatial resolution of the IR technique employed in this study and the smaller regions on the Ryugu samples relative to the meteorite samples studied with conventional FTIR techniques. In AFM-IR measurements (AFM-IR is a different type of near-field IR method; it employs thermal expansion of a sample by incident radiation and measures the deflection of an AFM cantilever probe as a result of the expansion), the IR signals from different depths could affect the obtained results. Namely, an AFM-IR spectrum may include signal originating from the materials below the top surface as well (down to >500 nm). In Kebukawa et al. (2019), the IR signals could be associated with depths down to several hundred nanometers below the sample surface; however, in our study with near-field IR, only surface signals (<30 nm) were detected. This difference could explain why the overlap between phyllosilicates and organic matter is not always observed in the case of Ryugu samples as in our study.

The morphological distribution of 1,250 cm^{-1} in A0030 (Figure 8d) and C0034 (Figure 8k) shows a significant difference (remarkably clear "discrete" and "diffuse" distribution). This may indicate that the 1,250 cm^{-1} signal of A0030 is derived from a different material than that in C0034. Since the 1,250 cm^{-1} distribution does not overlap with other organics (1,600 and 1,325 cm^{-1}), the 1,250 cm^{-1} compounds are potentially organic matter with C-O and/or N-H bonds and less aromatic or inorganic components. Interestingly, the 1,250 cm^{-1} peak observed in some of our Ryugu nano-FTIR spectra is absent in the IR absorption spectra of unheated carbonaceous chondrites (CI, CM, and CR) (Dartois et al., 2023; Kebukawa et al., 2023; Yabuta et al., 2023). In any case, the nature of this peak is not well understood at this time.

It is not clear whether the organic IR features are derived from macromolecular organic matter or smaller/soluble organic compounds. However, one possibility is that the organics overlapping with phyllosilicates could be soluble compounds present in the interlayer spaces; additionally, organics that did not overlap with phyllosilicates could be macromolecular materials, since the organic matter is known to be present in the interlayer spaces of phyllosilicates in Ryugu particles (Viennet et al., 2023).

5. Conclusions

The mineralogy and organic matter content of two Ryugu particles, A0030 (surface sample from TD1 and Chamber A) and C0034 (subsurface sample from TD2 and Chamber C), were studied by s-SNOM-based nano-FTIR spectroscopy and PsHet SNOM imaging at ~20 nm spatial resolution. Their chemical constituents were also examined by submicron-scale (~0.5 μm pixel size) confocal micro-Raman spectroscopy. Our investigation showed the detection and identification of abundant phyllosilicates, carbonates, and organic matter within both Ryugu particles. A0030 contains more serpentine-like mineralogy, whereas C0034 contains more saponite-like mineralogy. The presence of abundant phyllosilicates indicates extensive and heterogeneous aqueous alteration; however, the aqueous alteration on the parent asteroid was incomplete, as indicated by the presence of anhydrous silicates, such as olivine and pyroxene, in the Ryugu particles. The organic matter content of the Ryugu particles includes aromatic and aliphatic carbons, ketones, aldehydes, esters, amides, amines, and lactones. Due to the nanoscale spatial resolution employed in this work, organic-specific hotspots were detected. Wavelength-specific s-SNOM phase maps collected by utilizing the highly sensitive pseudoheterodyne detection principle show spatially resolved distribution maps of organic matter. The 1,250 cm^{-1} peak (the C-O/N-H vibrations in esters/carboxylic acids/amides) is strongly correlated with the 1,325 cm^{-1} peak (the C-O vibrations in esters) in both Ryugu grains; however, the former appears to exist as discrete grains in A0030, whereas it appears as a diffused component in C0034. Conversely, the opposite trend was observed for the 1,325 cm^{-1} peak; it appears as a diffused material in A0030 and was relatively more discrete in C0034. The absence of highly graphitic carbonaceous material in the Ryugu particles indicates that Ryugu did not experience elevated temperatures,

although A0030 experienced slightly higher temperatures than C0030, as determined via micro-Raman spectroscopy. While the exact reasons for the observed differences in the studied Ryugu particles are currently unknown, the differences in aqueous geochemistry, alteration temperature, pH, conditions, and/or original primary mineralogy could be responsible for heterogeneous silicate mineralogy. The differences in the organic matter likely reflect the inherent heterogeneity of the organic matter in Ryugu's parent asteroid. The identification of abundant nanoscale organic molecules within the Ryugu grains that could not be identified via micrometer-scale investigations emphasizes the importance of using the proper method when studying primitive solar system materials, such as the returned Ryugu particles and those that will be returned soon (such as OSIRIS-REx and MMX samples).

Data Availability Statement

The nano-FTIR and micro-Raman spectroscopic data as well as the nano-FTIR images presented in this work are archived at Zenodo.org (Yesiltas et al., 2023).

Acknowledgments
We thank JAXA and the curation team for allocating the A0030 and C0034 Ryugu asteroid particles. We also thank Attocube Systems and Şişecam Science and Technology Center for providing us instrument time. This work was also supported in part by the RISE2 node of NASA's Solar System Exploration Research Virtual Institute (SSERVI; PI: T. D. Glotch). The samples of ALH 85005, Y 980039, and GRA 95229 meteorites were provided by NASA-JSC. The sample of A 12236 meteorite was provided by NIPR.

References

Amarie, S., Ganz, T., & Keilmann, F. (2009). Mid-infrared near-field spectroscopy. *Optics Express*, *17*(24), 21794–21801. https://doi.org/10.1364/oe.17.021794

Amarie, S., Zaslansky, P., Kajihara, Y., Griesshaber, E., Schmahl, W. W., & Keilmann, F. (2012). Nano-FTIR chemical mapping of minerals in biological materials. *Beilstein Journal of Nanotechnology*, *3*(1), 312–323. https://doi.org/10.3762/bjnano.3.35

Barosch, J., Nittler, L. R., Wang, J., Alexander, C. M. D., De Gregorio, B. T., Engrand, C., et al. (2022). Presolar stardust in asteroid Ryugu. *The Astrophysical Journal Letters*, *935*(1), L3. https://doi.org/10.3847/2041-8213/ac83bd

Beyssac, O., Goffe´, B., Chopin, C., & Rouzaud, J. N. (2002). Raman spectra of carbonaceous material in metasediments, a new geothermometer. *Journal of Metamorphic Geology*, *20*(9), 859–871. https://doi.org/10.1046/j.1525-1314.2002.00408.x

Breitenfeld, L. B., Rogers, A. D., Glotch, T. D., Hamilton, V. E., Christensen, P. R., Lauretta, D. S., et al. (2021). Machine learning mid-infrared spectral models for predicting modal mineralogy of CI/CM chondritic asteroids and Bennu. *Journal of Geophysical Research: Planets*, *126*(12), e2021JE007035. https://doi.org/10.1029/2021je007035

Brunetto, R., Pino, T., Dartois, E., Cao, A. T., d'Hendecourt, L., Strazzulla, G., & Bréchignac, P. (2009). Comparison of the Raman spectra of ion irradiated soot and collected extraterrestrial carbon. *Icarus*, *200*(1), 323–337. https://doi.org/10.1016/j.icarus.2008.11.004

Busemann, H., Alexander, M. O. D., & Nittler, L. R. (2007). Characterization of insoluble organic matter in primitive meteorites by microRaman spectroscopy. *Meteoritics & Planetary Sciences*, *42*(7–8), 1387–1416. https://doi.org/10.1111/j.1945-5100.2007.tb00581.x

Cody, G. D., Yabuta, H., Kilcoyne, A. L. D., Araki, T., Ade, H., Dera, P., et al. (2008). Organic thermometry for chondritic parent bodies. *Earth and Planetary Science Letters*, *272*(1–2), 446–455. https://doi.org/10.1016/j.epsl.2008.05.008

Dartois, E., Kebukawa, Y., Yabuta, H., Mathurin, J., Engrand, C., Duprat, J., et al. (2023). Chemical composition of carbonaceous asteroid Ryugu from synchrotron spectroscopy in the mid-to far-infrared of Hayabusa2-returned samples. *Astronomy and Astrophysics*, *671*, A2. https://doi.org/10.1051/0004-6361/202244702

De Gregorio, B. T., Stroud, R. M., Nittler, L. R., Alexander, C. M. O. D., Bassim, N. D., Cody, G. D., et al. (2013). Isotopic and chemical variation of organic nanoglobules in primitive meteorites. *Meteoritics & Planetary Sciences*, *48*(5), 904–928. https://doi.org/10.1111/maps.12109

DellaGiustina, D. N., Kaplan, H. H., Simon, A. A., Bottke, W. F., Avdellidou, C., Delbo, M., et al. (2021). Exogenic basalt on asteroid (101955) Bennu. *Nature Astronomy*, *5*(1), 31–38. https://doi.org/10.1038/s41550-020-1195-z

Ferrari, A. C., & Robertson, J. (2000). Interpretation of Raman spectra of disordered and amorphous carbon. *Physical Review B*, *61*(20), 14095–14107. https://doi.org/10.1103/physrevb.61.14095

Garvie, L. A. J., Baumgardner, G., & Buseck, P. R. (2008). Scanning electron microscopical and cross-sectional analysis of extraterrestrial carbonaceous nanoglobules. *Meteoritics & Planetary Sciences*, *43*(5), 899–903. https://doi.org/10.1111/j.1945-5100.2008.tb01088.x

Greenwood, R. C., Franchi, I. A., Findlay, R., Malley, J. A., Ito, M., Yamaguchi, A., et al. (2023). Oxygen isotope evidence from Ryugu samples for early water delivery to Earth by CI chondrites. *Nature Astronomy*, *7*(1), 29–38. https://doi.org/10.1038/s41550-022-01824-7

Hamilton, V. E., Christensen, P. R., Kaplan, H. H., Haberle, C. W., Rogers, A. D., Glotch, T. D., et al. (2021). Evidence for limited compositional and particle size variation on asteroid (101955) Bennu from thermal infrared spectroscopy. *Astronomy and Astrophysics*, *650*, A120. https://doi.org/10.1051/0004-6361/202039728

Hirakawa, N., Kebukawa, Y., Kobayashi, K., & Nakano, H. (2021). Effects of minerals on metamorphism of organic matter during thermal processes in meteorite parent bodies. *Icarus*, *358*, 114167. https://doi.org/10.1016/j.icarus.2020.114167

Homma, Y., Kouketsu, Y., Kagi, H., Mikouchi, T., & Yabuta, H. (2015). Raman spectroscopic thermometry of carbonaceous material in chondrites: Four–band fitting analysis and expansion of lower temperature limit. *Journal of Mineralogical and Petrological Sciences*, *110*(6), 276–282. https://doi.org/10.2465/jmps.150713a

Huth, F., Govyadinov, A., Amarie, S., Nuansing, W., Keilmann, F., & Hillenbrand, R. (2012). Nano-FTIR absorption spectroscopy of molecular fingerprints at 20 nm spatial resolution. *Nano Letters*, *12*(8), 3973–3978. https://doi.org/10.1021/nl301159v

Huth, F., Schnell, M., Wittborn, J., Ocelic, N., & Hillenbrand, R. (2011). Infrared-spectroscopic nanoimaging with a thermal source. *Nature Materials*, *10*(5), 352–356. https://doi.org/10.1038/nmat3006

Ito, M., Tomioka, N., Uesugi, M., Yamaguchi, A., Shirai, N., Ohigashi, T., et al. (2022). A pristine record of outer Solar System materials from asteroid Ryugu's returned sample. *Nature Astronomy*, *6*(10), 1163–1171. https://doi.org/10.1038/s41550-022-01745-5

Jakubek, R. S., & Fries, M. D. (2023). Laser Raman induced degradation of macromolecular carbon in coals and meteorites. *Earth and Space Science*, *10*(6), e2022EA002724. https://doi.org/10.1029/2022ea002724

Kebukawa, Y., Kobayashi, H., Urayama, N., Baden, N., Kondo, M., Zolensky, M. E., & Kobayashi, K. (2019). Nanoscale infrared imaging analysis of carbonaceous chondrites to understand organic-mineral interactions during aqueous alteration. *Proceedings of the National Academy of Sciences of the United States of America*, *116*(3), 753–758. https://doi.org/10.1073/pnas.1816265116

Kebukawa, Y., Nakashima, S., Ishikawa, M., Aizawa, K., Inoue, T., Nakamura-Messenger, K., & Zolensky, M. E. (2010). Spatial distribution of organic matter in the Bells CM2 chondrite using near-field infrared microspectroscopy. *Meteoritics & Planetary Sciences*, *45*(3), 394–405. https://doi.org/10.1111/j.1945-5100.2010.01030.x

Kebukawa, Y., Quirico, E., Dartois, E., Yabuta, H., Bejach, L., Bonal, L., et al. (2023). Infrared absorption spectra from organic matter in the asteroid Ryugu samples: Some unique properties compared to unheated carbonaceous chondrites. *Meteoritics & Planetary Sciences*. in press. https://doi.org/10.1111/maps.14064

Kouketsu, Y., Mizukami, T., Mori, H., Endo, S., Aoya, M., Hara, H., et al. (2014). A new approach to develop the Raman carbonaceous material geothermometer for low-grade metamorphism using peak width. *Island Arc*, *23*(1), 33–50. https://doi.org/10.1111/iar.12057

Mastel, S., Govyadinov, A. A., Maissen, C., Chuvilin, A., Berger, A., & Hillenbrand, R. (2018). Understanding the image contrast of material boundaries in IR nanoscopy reaching 5 nm spatial resolution. *ACS Photonics*, *5*(8), 3372–3378. https://doi.org/10.1021/acsphotonics.8b00636

Morlok, A., Hamann, C., Martin, D., Weber, I., Joy, K. H., Hiesinger, H., et al. (2020). Mid-infrared spectroscopy of laser-produced basalt melts for remote sensing application. *Icarus*, *335*, 113410. https://doi.org/10.1016/j.icarus.2019.113410

Nakamura, E., Kobayashi, K., Tanaka, R., Kunihiro, T., Kitagawa, H., Potiszil, C., et al. (2022). On the origin and evolution of the asteroid Ryugu: A comprehensive geochemical perspective. *Proceedings of the Japan Academy, Series B*, *98*(6), 227–282. https://doi.org/10.2183/pjab.98.015

Nakamura, T., Matsumoto, M., Amano, K., Enokido, Y., Zolensky, M. E., Mikouchi, T., et al. (2022). Formation and evolution of carbonaceous asteroid Ryugu: Direct evidence from returned samples. *Science*, *379*(6634), eabn8671. https://doi.org/10.1126/science.abn8671

Nakamura-Messenger, K., Messenger, S., Keller, L. P., Clemett, S. J., & Zolensky, M. E. (2006). Organic globules in the Tagish Lake meteorite: Remnants of the protosolar disk. *Science*, *314*(5804), 1439–1442. https://doi.org/10.1126/science.1132175

Naraoka, H., Takano, Y., Dworkin, J. P., Oba, Y., Hamase, K., Furusho, A., et al. (2023). Soluble organic molecules in samples of the carbonaceous asteroid (162173) Ryugu. *Science*, *379*(6634), eabn9033. https://doi.org/10.1126/science.abn9033

Nasse, M. J., Mattson, E. C., Reininger, R., Kubala, T., Janowski, S., El-Bayyari, Z., & Hirschmugl, C. J. (2011). Multi-beam synchrotron infrared chemical imaging with high spatial resolution: Beamline realization and first reports on image restoration. *Nuclear Instruments and Methods in Physics Research Section A: Accelerators, Spectrometers, Detectors and Associated Equipment*, *649*(1), 172–176. https://doi.org/10.1016/j.nima.2010.12.095

Nguyen, A. N., Mane, P., Keller, L. P., Piani, L., Abe, Y., Aléon, J., et al. (2023). Abundant presolar grains and primordial organics preserved in carbon-rich exogenous clasts in asteroid Ryugu. *Science Advances*, *9*(28), eadh1003. https://doi.org/10.1126/sciadv.adh1003

Ocelic, N., Huber, A., & Hillenbrand, R. (2006). Pseudoheterodyne detection for background-free near-field spectroscopy. *Applied Physics Letters*, *89*(10). https://doi.org/10.1063/1.2348781

Pilorget, C., Okada, T., Hamm, V., Brunetto, R., Yada, T., Loizeau, D., et al. (2022). First compositional analysis of Ryugu samples by the MicrOmega hyperspectral microscope. *Nature Astronomy*, *6*(2), 221–225. https://doi.org/10.1038/s41550-021-01549-z

Sadezky, A., Muckenhuber, H., Grothe, H., Niessner, R., & Pöschl, U. (2005). Raman microspectroscopy of soot and related carbonaceous materials: Spectral analysis and structural information. *Carbon*, *43*(8), 1731–1742. https://doi.org/10.1016/j.carbon.2005.02.018

Salisbury, J. W., D'Aria, D. M., & Jarosewich, E. (1991). Midinfrared (2.5–13.5 μm) reflectance spectra of powdered stony meteorites. *Icarus*, *92*(2), 280–297. https://doi.org/10.1016/0019-1035(91)90052-u

Schmidt, J. S., & Hinrichs, R. (2020). Evaluation of terrestrial carbonaceous matter aromatization by Raman spectroscopy and its application to C chondrites. *Meteoritics & Planetary Sciences*, *55*(4), 800–817. https://doi.org/10.1111/maps.13467

Starkey, N. A., Franchi, I. A., & Alexander, C. M. O. 'D. (2013). A Raman spectroscopic study of organic matter in interplanetary dust particles and meteorites using multiple wavelength laser excitation. *Meteoritics & Planetary Sciences*, *48*(10), 1800–1822. https://doi.org/10.1111/maps.12196

Suzuki, A., Yamanoi, Y., Nakamura, T., & Nakashima, S. (2010). Micro-spectroscopic characterization of organic and hydrous components in weathered Antarctic micrometeorites. *Earth Planets and Space*, *62*(1), 33–46. https://doi.org/10.5047/eps.2008.11.001

Tachibana, S., Sawada, H., Okazaki, R., Takano, Y., Sakamoto, K., Miura, Y. N., et al. (2022). Pebbles and sand on asteroid (162173) Ryugu: In situ observation and particles returned to Earth. *Science*, *375*(6584), 1011–1016. https://doi.org/10.1126/science.abj8624

Tuinstra, F., & Koenig, J. L. (1970). Raman spectrum of graphite. *The Journal of Chemical Physics*, *53*(3), 1126–1130. https://doi.org/10.1063/1.1674108

Viennet, J. C., Le Guillou, C., Remusat, L., Baron, F., Delbes, L., Blanchenet, A. M., et al. (2022). Experimental investigation of Fe-clay/organic interactions under asteroidal conditions. *Geochimica et Cosmochimica Acta*, *318*, 352–365. https://doi.org/10.1016/j.gca.2021.12.002

Viennet, J. C., Roskosz, M., Nakamura, T., Beck, P., Baptiste, B., Lavina, B., et al. (2023). Interaction between clay minerals and organics in asteroid Ryugu. *Geochemical Perspectives Letters*, *25*, 8–12. https://doi.org/10.7185/geochemlet.2307

Vinogradoff, V., Le Guillou, C., Bernard, S., Viennet, J. C., Jaber, M., & Remusat, L. (2020). Influence of phyllosilicates on the hydrothermal alteration of organic matter in asteroids: Experimental perspectives. *Geochimica et Cosmochimica Acta*, *269*, 150–166. https://doi.org/10.1016/j.gca.2019.10.029

Visser, R., John, T., Menneken, M., Patzek, M., & Bischoff, A. (2018). Temperature constraints by Raman spectroscopy of organic matter in volatile-rich clasts and carbonaceous chondrites. *Geochimica et Cosmochimica Acta*, *241*, 38–55. https://doi.org/10.1016/j.gca.2018.08.037

Yabuta, H., Cody, G. D., Engrand, C., Kebukawa, Y., De Gregorio, B., Bonal, L., et al. (2023). Macromolecular organic matter in samples of the asteroid (162173) Ryugu. *Science*, *379*(6634). eabn9057. https://doi.org/10.1126/science.abn9057

Yada, T., Abe, M., Okada, T., Nakato, A., Yogata, K., Miyazaki, A., et al. (2022). Preliminary analysis of the Hayabusa2 samples returned from C-type asteroid Ryugu. *Nature Astronomy*, *6*(2), 214–220. https://doi.org/10.1038/s41550-021-01550-6

Yesiltas, M., Glotch, D. T., Kebukawa, Y., Sava, B., Durmaz, Y., & Northrup, P. (2023). Nanoscale spectroscopic identification and characterization of minerals and organic matter in Ryugu particles (Version 1) [Dataset]. *Zenodo*. https://doi.org/10.5281/zenodo.10650031

Yesiltas, M., Glotch, T. D., & Kaya, M. (2021). Nanoscale infrared characterization of dark clasts and fine-Grained Rims in CM2 chondrites: Aguas Zarcas and Jbilet Winselwan. *ACS Earth and Space Chemistry*, *5*(12), 3281–3296. https://doi.org/10.1021/acsearthspacechem.1c00290

Yesiltas, M., Glotch, T. D., & Sava, B. (2021). Nano-FTIR spectroscopic identification of prebiotic carbonyl compounds in Dominion Range 08006 carbonaceous chondrite. *Scientific Reports*, *11*(1), 11656. https://doi.org/10.1038/s41598-021-91200-8

Yesiltas, M., & Kebukawa, Y. (2016). Associations of organic matter with minerals in Tagish Lake meteorite via high spatial resolution synchrotron-based FTIR microspectroscopy. *Meteoritics & Planetary Sciences*, *51*(3), 584–595. https://doi.org/10.1111/maps.12609

Yesiltas, M., Kebukawa, Y., Peale, R. E., Mattson, E., Hirschmugl, C. J., & Jenniskens, P. (2014). Infrared imaging spectroscopy with micron resolution of Sutter's Mill meteorite grains. *Meteoritics & Planetary Sciences*, *49*(11), 2027–2037. https://doi.org/10.1111/maps.12321

Yesiltas, M., Peale, R. E., Unger, M., Sedlmair, J., & Hirschmugl, C. J. (2015). Organic and inorganic correlations for Northwest Africa 852 by synchrotron-based Fourier transform infrared microspectroscopy. *Meteoritics & Planetary Sciences*, *50*(10), 1684–1696. https://doi.org/10.1111/maps.12498

Yesiltas, M., Young, J., & Glotch, T. D. (2021). Thermal metamorphic history of Antarctic CV3 and CO3 chondrites inferred from the first-and second-order Raman peaks of polyaromatic organic carbon. *American Mineralogist: Journal of Earth and Planetary Materials*, *106*(4), 506–517. https://doi.org/10.2138/am-2021-7507

Yokoyama, T., Nagashima, K., Nakai, I., Young, E. D., Abe, Y., Aleon, J., et al. (2022). Samples returned from the asteroid Ryugu are similar to Ivuna-type carbonaceous meteorites. *Science*, *379*(6634), eabn7850. https://doi.org/10.1126/science.abn7850

Young, J. M., Glotch, T. D., Yesiltas, M., Hamilton, V. E., Breitenfeld, L. B., Bechtel, H. A., et al. (2022). Nano-FTIR investigation of the CM chondrite allan Hills 83100. *Journal of Geophysical Research: Planets*, *127*(5), e2021JE007166. https://doi.org/10.1029/2021je007166